Università degli Studi della Basilicata

DOTTORATO DI RICERCA IN

Ingegneria per l'Innovazione e lo Sviluppo Sostenibile

Development of a versatile ground-based UV lidar prototype, featuring a CO_2 Raman channel, in support of the ASI-NASA CALIGOLA mission

FIS-01
FIS-06

Dottorando:
Marco Di Paolantonio

Relatore:
Prof. Paolo Di Girolamo

Correlatore:
Dott. Davide Dionisi

Coordinatrice del Dottorato:
Prof.ssa Aurelia Sole

XXXVII Ciclo

Contents

Abstract

This thesis investigates the development and application of Raman lidar systems for measuring atmospheric compositional and thermodynamic properties. The research focuses on two ground-based lidar prototypes, CONCERNING and MARCO, developed during the PhD program. These systems, utilizing both rotational and vibrational Raman lidar techniques in the UV spectrum, incorporate advanced technologies for laser emission, spectral selection, optical signal detection, and data acquisition. Housed in rugged, weather-resistant containers with remote control capabilities, these lidars offer continuous and unattended measurement capabilities. MARCO, notably, is the first lidar prototype that demonstrates the feasibility of a Raman lidar based on a micro-pulse laser source.

The two lidar systems were deployed in various national and international measurement campaigns, such as WaLiNeAs, BELLA, and DECIPHER, highlighting their capabilities in studying extreme precipitation events, characterizing the atmospheric boundary layer, and investigating transport and mixing phenomena in mountain areas. Future campaigns are planned to further explore marine aerosol and cloud interaction.

As part of the research project, a Raman lidar simulator was developed to define the characteristics of the spectral selection devices required for CO_2 mixing ratio measurements, evaluate system performance, and calibrate the measurements through an original technique, taking advantage of day-time lidar background signal. The CO_2 measurement capability was successfully implemented in the CONCERNING lidar, with promising results demonstrated through calibrated measurements compared to satellite data.

The thesis contributes significantly to the CALIGOLA (Cloud Aerosol LIdar for Global scale observations of the Ocean-Land-Atmosphere system) satellite mission, a collaborative project between the Italian Space Agency and NASA, with the University of Basilicata representing the focal point for the scientific activities. The research provided valuable insights into the Raman lidar technique and served as a testing platform for state-of-the-art technological solutions and techniques that will be implemented in the CALIGOLA mission. The developed lidar simulator will be enhanced to form the foundation of a comprehensive end-to-end lidar simulator of the space-borne lidar. Additionally, the two lidar systems' measurement capabilities will be instrumental in calibrating and validating CALIGOLA's atmospheric products and will support future synergetic studies, enhancing the understanding of feedback and coupling mechanisms within Earth's biogeochemical cycles.

Introduction

Our understanding of the Earth water, energy and carbon cycles still shows gaps on all temporal and spatial scales [1, 2]. Despite recent advancements, this is mainly due to the lack of accurate measurements of carbon dioxide (CO_2) and thermodynamic (TD) profiles, that is, water vapor (WV) and temperature profiles, with high temporal and spatial resolution, especially in the lower troposphere.

The concentration of CO_2 in the atmosphere has reached values above 420 ppm, with an average annual growth rate of about 2.5 ppm; this is already having major effects on the Earth's climate and a great effort has been made over the years to predict future trends. Part of the emissions are absorbed by various natural sinks [3] whose better quantification is necessary to accurately simulate possible future scenarios. Land carbon sinks uncertainty is the highest among all flux components, consequently, accurate means to monitor land sinks are required. While CO_2 has relatively uniform vertical distribution and therefore its total atmospheric content is well monitored by in-situ as well as satellite measurements, the correct quantitative knowledge of source/sink processes, that occurs mostly close to surface, requires a vertically detailed sampling as well as sub diurnal temporal sampling [4].

The availability of accurate CO_2 profiles with high vertical and temporal sampling, as those that could be provided by ground-based Raman lidars, has the potential to impact climate research and modelling. For example, these measurements could contribute to overcome some of the present gaps in the comprehension of CO_2 sink mechanisms by the biosphere (like the evaluation of forests' carbon capturing capabilities) and estimating land-atmosphere feedback mechanisms [5]. Although the space and ground network for CO_2 monitoring has regularly expanded over the past years, it does not guarantee the necessary spatial and temporal resolution needed for a quantitative analysis of sources and sinks. Additionally, presently operational space sensors provide CO_2 measurements above forest canopies, which do not allow to properly estimate Gross Primary Production, that is, the total amount of carbon fixed with plant photosynthesis [6].

Accurate, high-resolution observations of TD profiles are instead essential for improving weather forecasting and re-analyses [7, 8], for studying land-atmosphere feedback processes and for improving model parameterizations of land-surface and turbulent transport processes in the Atmospheric Boundary Layer (ABL) [9, 10].

The combined measurement of these compositional and thermodynamic properties of the atmosphere is important to improve the understanding of feedbacks and coupling mechanisms in biogeochemical cycles of the Earth system.

In the last decades, the Raman lidar technique has proved to be a valuable tool to provide profiles of a variety of important atmospheric variables, with the advantage of providing

continuous monitoring of the sensed parameters, with high measurement accuracy/precision and spatial/temporal resolution, and a high level of independence between measured variables [11–13].

By combining vibrational and rotational Raman backscatter signals, simultaneous measurements of water vapor, CO_2, and temperature profiles, and a variety of derived variables (for example, aerosol backscatter and extinction profiles, ABL height, cloud top heights, cloud optical depth) are possible with unprecedented spatial and temporal resolution. The CALIGOLA (Cloud Aerosol LIdar for Global scale observations of the Ocean-Land-Atmosphere system) satellite mission [14], funded by the Italian Space Agency (ASI) in collaboration with the National Aeronautics and Space Administration (NASA), with the University of Basilicata representing the focal point for the scientific activities, and the mentor of my thesis being the Principal Investigator of the mission, aims at addressing these observational gaps with a state-of-the-art active remote sensing system based on the Raman lidar technique. The CONCERNING (COmpact RamaN lidar for Atmospheric CO_2 and ThERmodyNamic ProfilING) research project, funded to the University of Basilicata through "Fondo Integrativo Speciale per la Ricerca" by the Italian Ministry of University and Research, has represented the framework for the development of a ground demonstrator for these advanced measurement capabilities. The research conducted as part of my PhD program and reported in this dissertation is integral to and supported by these projects, and the activities described in this thesis aim at contributing to these ambitious objectives.

The above-mentioned projects will take advantage of different instrumental characteristics, providing a variety of geophysical products.

Specifically, in the current design, the ASI-NASA CALIGOLA mission will take advantage of elastic, Raman, and fluorescent lidar signals in the ultraviolet (UV), visible (VIS) and near infrared (NIR), with objectives that includes both atmospheric and oceanic observations.

In the frame of the project CONCERNING, a versatile and transportable Raman lidar was developed to provide accurate and high-resolution measurements of the vertical profiles of CO_2, water vapor mixing ratio, temperature and particle backscattering/extinction profiles, with the temporal and spatial resolution needed to resolve convective scales and turbulent processes.

Moreover, a second Raman lidar MARCO (Micropulse Atmospheric Optical Radar for Climate Observations), the first micro-pulse lidar able to provide water vapor mixing ratio, temperature, and aerosol backscatter and extinction coefficient profiles, was developed and tested.

Objective of the research project described in this thesis is to investigate the feasibility and the limits of Raman lidar systems dedicated to the measurement of the aforementioned parameters, with a particular focus on the CO_2 measurements. This objective was accomplished through parallel activities of modelling and instrument design, development, testing and validation. Moreover, the two developed lidar prototypes served also as a testbed for several state-of-the-art solutions and techniques that will be adopted in the CALIGOLA mission. The work was carried out within the

frame of the activities of the Lidar Group at Scuola di Ingegneria (SI-UniBas) of the University of Basilicata, in tight cooperation with ISMAR-CNR and "Sapienza" University of Rome.

The Raman lidar technique has been investigated over the past decades for its application in CO_2 profile measurements [12, 15–18]. Despite its high potential, the technique faced challenges due to the low signal-to-noise ratio (SNR) associated with the CO_2 ro-vibrational Raman signals. However, recent advancements in laser technology, as well as improvements in spectral selection and signal detection devices, have renewed interest in the technique, leading to the development of a new generation of lidar systems specifically designed for its exploitation. The instrument design process was supported by a Raman lidar simulator. This tool accurately simulates, in a spectrally resolved manner, all laser light interaction mechanisms with atmospheric constituents, as well as all the devices present in the considered Raman lidar experimental setup. The developed simulator supported the definition of the specifications of the spectral selection device. In particular, the use of additional channels was evaluated, and the optimal characteristics (position of the central wavelength and bandwidth) of the interferential filter used as spectral selection device were determined. To maximize the system performances, different options for the spectral selection of the CO_2 vibrational Raman signals were verified, and a consolidated design has been defined, implemented and tested.

The thesis is structured as follows. Chapter 1 introduces and describes the Raman lidar simulator, used for the definition of the spectral selection devices, in the evaluation of the system performances, and in the calibration of the CO_2 measurements. The preliminary simulations are then detailed in Chapter 2. The two Raman lidar systems CONCERNING and MARCO, developed and tested during the research project, are described in Chapter 3. The result of several national and international field campaigns, demonstrating the prototypes' measurement capabilities are shown in Chapter 5. The CONCERNING measurement capabilities of CO_2 mixing ratio profiles, taking advantage of a novel calibration technique, are demonstrated in Chapter 6. Finally, the impact of present and future activities in support of the CALIGOLA mission are detailed in Chapter 7.

1 Raman lidar simulator

In order to define the characteristics of the interference filters needed for the measurement of CO_2 profiles and to assess the potential performance of a lidar system designed for this purpose, a Raman lidar simulator was developed. The code consists of a radiative transfer model (RTM) able to simulate, in a spectrally resolved manner, all relevant laser light interaction mechanisms with atmospheric constituents, and the echoes produced by these constituents, the behaviour of all the devices present in the considered Raman lidar experimental setup, and the electromagnetic signal associated with the environmental background radiation (primarily sun radiation).

A detailed explanation of the equations and parameters used in the simulator is here provided in what follows.

1.1 Lidar signal

The elastic backscattered signal at the laser wavelength λ_0, expressed as number of detected photons per laser shot and range bin, can be calculated as [19]:

$$P_{\lambda_0}(z) = P_0 \cdot \eta(\lambda_0)\tau(\lambda_0)\epsilon(\lambda_0) \cdot \frac{A}{z^2} \cdot [\beta_{\mathrm{mol}}(z) + \beta_{\mathrm{aer}}(z)] \cdot T^2(\lambda_0, z)\, \Delta z \qquad (1)$$

where z is the distance between the scattering volume and the receiver, which for a ground-based lidar pointing at the zenith corresponds to the altitude above ground level, $\Delta z = c\Delta t/2$ is the vertical resolution, where Δt is the sampling resolution, $P_0 = E_0/(hc/\lambda_0)$ is the number of emitted photons, calculated as the single pulse energy E_0 divided by the energy of the photon, η is the overall optical transmission efficiency not taking into account the interference filter transmission τ, ϵ is the detector quantum efficiency, A is the telescope primary mirror area, $T(\lambda, z)$ is the atmospheric transmissivity. Finally, $\beta_{\mathrm{mol}}(z)$ and $\beta_{\mathrm{aer}}(z)$ are the elastic molecular and aerosol backscatter coefficients from the scattering volume at distance z, respectively.

The ro-vibrational Raman signals for a spectral bin with central wavelength λ and bandwidth $\Delta\lambda$ can be estimated as:

$$P(\lambda, z) = P_0 \cdot \eta(\lambda)\tau(\lambda)\epsilon(\lambda) \cdot \frac{A}{z^2} \cdot \left(\sum_i n_i(z) \cdot \frac{d\sigma_i}{d\Omega}\right) \cdot T(\lambda, z)T(\lambda_0, z)\, \Delta z \qquad (2)$$

where $n_i(z)$ and $\frac{d\sigma_i}{d\Omega}$ are the numerical densities of the atmospheric species generating the ro-vibrational Raman scattering effect (primarily, molecular nitrogen and oxygen, water vapor, and carbon dioxide) and the differential cross section of the *i*-th rotational Raman line falling in the spectral bandwidth Δλ, respectively. The product of these two quantities gives the Raman backscatter coefficient (see Figure 2). The total signal received in a given lidar channel is the sum of the $P(\lambda, z)$ calculated over the relative filter transmission curve.

1.1.1 Transmissivity

The atmospheric transmissivity $\mathrm{T}(\lambda, \mathrm{z})$, approximated as a discrete sum, is calculated as:

$$\mathrm{T}(\lambda, \mathrm{z}) = \exp[-\textstyle\sum_{\mathrm{i}} \alpha(\lambda, \mathrm{z_i})\Delta \mathrm{z}] \qquad (3)$$

with a sum over all z_{i} values from ground to $z_i = z$ where $\alpha(\lambda, z) = \alpha_{mol}(\lambda, z) + \alpha_{aer}(\lambda, z) + \alpha_{gas}(\lambda, z)$ is the extinction coefficient.

The molecular extinction coefficient is calculated as $\alpha_{mol}(\lambda, z) = \mathrm{n(z)}\sigma_{\mathrm{mol}}(\lambda)$ where the Rayleigh scattering cross section $\sigma_{\mathrm{mol}}(\lambda)$ is calculated as in [20].

Aerosol extinction coefficient is computed from a parametrized representation based on aerosol optical thickness τ_{380}, Angstrom exponent AE and a scale height h, having assumed an exponential decrease of the aerosol concentration:

$$\alpha_{aer}(\lambda, z) = \left(\frac{\lambda}{380}\right)^{-AE} \cdot \frac{\tau_{380}}{h} \exp\left(-\frac{z}{h}\right) \qquad (4)$$

The gas absorption coefficients are calculated from temperature and wavelength dependent tabulated cross sections as $\alpha_{gas}(\lambda, z) = \sum_i \mathrm{n_i}(z)\sigma_i(\lambda)$ where i is the gas species considered, in particular O_3 [21], NO_2 [22], and SO_2 [23]. The atmospheric density profiles for the molecular and gas cross sections are the AFGL atmospheric constituent profiles [24].

1.1.2 Elastic backscatter coefficients

As in narrowband filters with sub-nm bandwidths the contribution to the signal comes primarily from the Cabannes line and not from all the Rayleigh scattering (that is, Cabannes + rotational Raman), the molecular backscattering coefficient was calculated as:

$$\beta_{mol} = \sum_{N_2,O_2} \rho_{N_2,O_2} \left(\frac{d\sigma}{d\Omega}\right)^{Cabannes} \tag{5}$$

where ρ_{N_2,O_2} is the numerical density of N_2 or O_2 and $\left(\frac{d\sigma}{d\Omega}\right)^{Cabannes}$ is the Cabannes differential backscattering cross section of the relative molecular species [25]:

$$\left(\frac{d\sigma}{d\Omega}\right)^{Cabannes} = \left(\frac{\pi}{\epsilon_0}\right)^2 \tilde{\nu}_0^4 \left(a^2 + \frac{7}{180}\gamma^2\right) \tag{6}$$

where $\tilde{\nu}_0$ is the wavenumber corresponding to the emission wavelength λ_0, a is the mean polarizability, and is the anisotropy of the polarizability. These molecular constants are listed in Table 1. Please note that the factor $(4\pi\varepsilon_0)^2$ is there indicated separately in order to show the original values from the literature. These values have to be divided by $(4\pi\varepsilon_0)^2$ or, in alternative, the term $\left(\frac{\pi}{\epsilon_0}\right)^2$ in Equation (6) has to be replaced by $(2\pi)^4$.

Table 1: Molecular constants for the calculation of Cabannes, rotational Raman, and ro-vibrational Raman scattering cross sections of molecular nitrogen and oxygen [25].

	a^2 [$m^6/(4\pi\varepsilon_0)^2$]	γ^2 [$m^6/(4\pi\varepsilon_0)^2$]	a'^2 [$m^4/kg/(4\pi\varepsilon_0)^2$]	γ'^2 [$m^4/kg/(4\pi\varepsilon_0)^2$]
N_2	$3.17\cdot10^{-60}$	$0.52\cdot10^{-60}$	$2.62\cdot10^{-14}$	$4.23\cdot10^{-14}$
O_2	$2.66\cdot10^{-60}$	$1.26\cdot10^{-60}$	$1.63\cdot10^{-14}$	$6.46\cdot10^{-14}$

The aerosol backscattering coefficient was instead calculated from the aerosol extinction coefficient as:

$$\beta_{aer} = \frac{\alpha_{aer}}{LR} \tag{7}$$

where LR is the so-called particle lidar ratio, assuming values between 20 and 100 sr depending on the aerosol type [25].

1.1.3 Raman cross sections

Raman scattering is an inelastic process that leads to a change in the scattering molecule's rotational and/or ro-vibrational quantum state (Figure 1). If the molecule absorbs energy, the scattered photon is red-shifted by an amount $\Delta\tilde{\nu}$ and the process is known as Stokes Raman scattering. If the molecule transfers energy to the photon, this is blue-shifted and the process is known as anti-Stokes Raman scattering.

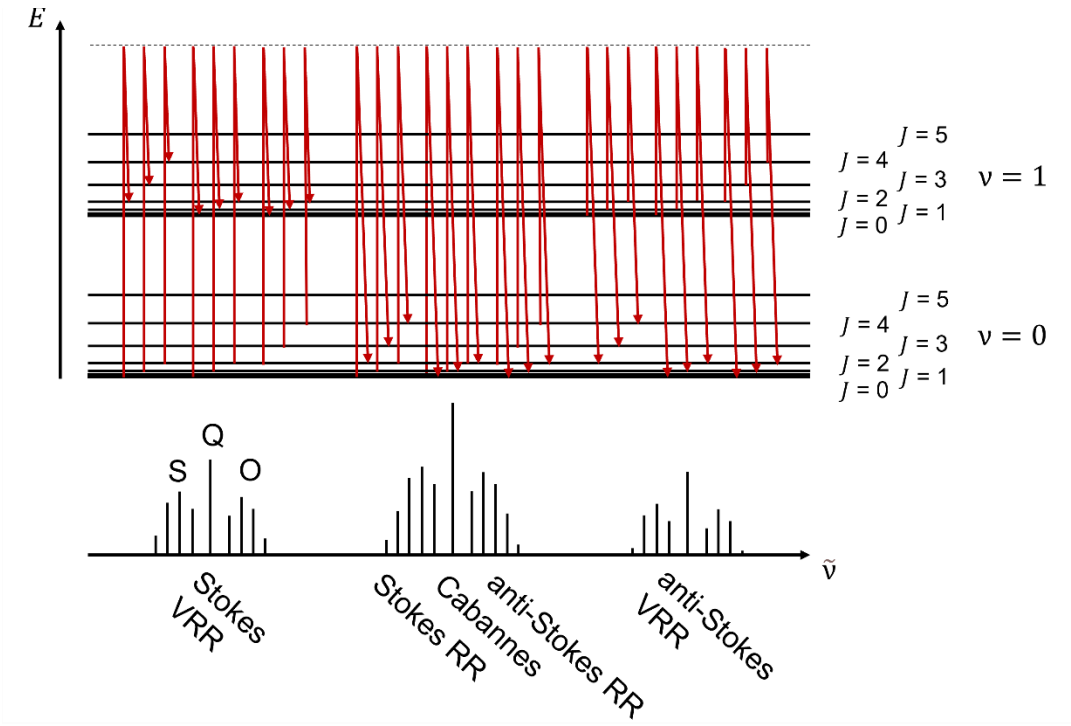

Figure 1: Schematic representation of Ro-vibrational energy levels of the N_2 molecule, Raman transitions, and resulting spectrum.

The Raman backscattering differential cross sections (and consequently the relative backscatter coefficients representative of the intensity of the correspondent lidar signal, see Figure 2) are calculated line-by-line for the different molecular species of the atmosphere.

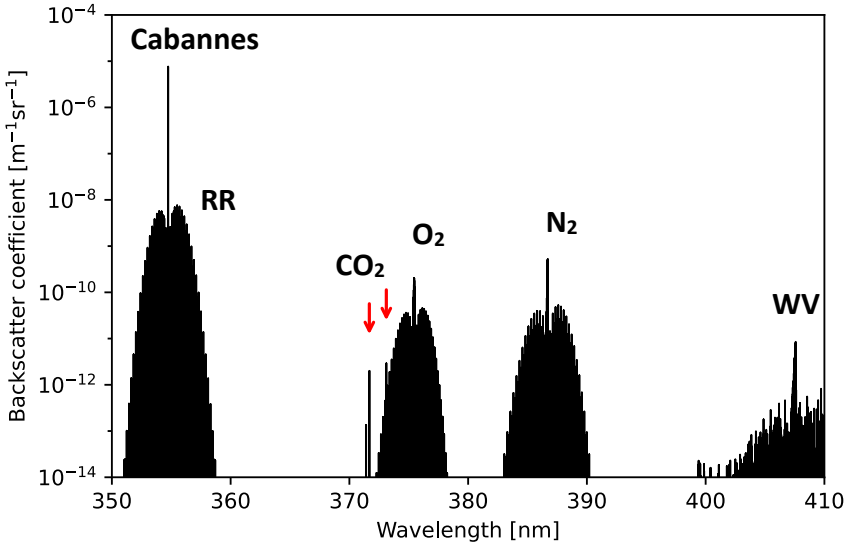

Figure 2: Simulated Cabannes, anti-Stokes and Stokes rotational Raman (RR), and Stokes ro-vibrational Raman spectrum for standard atmosphere at 1020 hPa, 300 K, CO_2 concentration of 415 ppm, and water vapor mixing ratio of 10 g/kg.

1.1.3.1 **Nitrogen and oxygen**

The energy levels and Raman backscattering differential cross sections can be directly calculated for homonuclear diatomic molecules such as N_2 and O_2 [25].

For such molecules the model of a free rotating harmonic oscillator gives for the vibrational energy levels:

$$E_{vib,\nu} = \mathrm{h}c\tilde{\nu}_{vib}\left(\nu + \frac{1}{2}\right) \tag{8}$$

where $\tilde{\nu}_{vib}$ is the oscillator frequency of the molecule, and $\nu = 0,1,2,\ldots$ is the vibrational quantum number.

The rotational energies can be instead approximated as:

$$E_{rot,J,\nu} = \mathrm{h}c[B_\nu J(J+1) - D_\nu J^2(J+1)^2] \tag{9}$$

where $J = 0,1,2,\ldots$ is the rotational quantum number, B_ν is the rotational constant, and D_ν is the centrifugal distortion that takes into account the stretching of the molecule due to rotation. The constants $\tilde{\nu}_{vib}$, B_ν, and D_ν are listed in Table 2.

Table 2: Rotational and ro-vibrational molecular constants used for the calculation of nitrogen and oxygen energy levels [25, 26].

	$\tilde{\nu}_{vib}$ [cm^{-1}]	B_0 [cm^{-1}]	B_1 [cm^{-1}]	D_0 [cm^{-1}]	D_1 [cm^{-1}]
N_2	2330.7	1.98957	1.97219	$5.7606 \cdot 10^{-6}$	$5.7610 \cdot 10^{-6}$
O_2	1556.4	1.43768	1.42188	$4.85 \cdot 10^{-6}$	$4.864 \cdot 10^{-6}$

Given the selection rules for vibrational and rotational Raman transitions $\Delta\nu = 0, \pm 1$ and $\Delta J = 0, \pm 2$, Raman frequency shifts can be finally calculated from the ro-vibrational energy levels as:

$$\Delta\tilde{\nu} = \tilde{\nu}_f - \tilde{\nu}_i = \frac{\Delta E}{hc} \tag{10}$$

The differential cross section for each Raman line can be calculated as:

$$\frac{d\sigma}{d\Omega} = \left(\frac{\pi}{\epsilon_0}\right)^2 (\tilde{\nu}_0 + \Delta\tilde{\nu})^4 \frac{g_J \Phi_J}{Q(T)} \exp\left[-\frac{B_\nu hcJ(J+1)}{k_B T}\right] \tag{11}$$

where J and ν are the initial ro-vibrational state quantum numbers, Q is the partition function, approximated as:

$$Q(T) = \frac{(2I+1)^2 k_B T}{2hcB_0} \tag{12}$$

where $I_{N_2} = 1$ and $I_{O_2} = 0$ is the nuclear spin quantum number, which leads to different nuclear spin statistics for the two molecules.

The statistical weight factor g_J values for N_2 are $g_J = 6$ for J even and $g_J = 3$ for J odd; while for O_2, $g_J = 0$ for J even and $g_J = 1$ for J odd. This condition results in N_2 Raman lines showing an alternating intensity and in O_2 having every second line missing.

The term Φ_J contains the Placzek–Teller coefficients, the degeneracy $2J + 1$, and a factor for the specific observational geometry.

For Stokes rotational lines ($\Delta\nu = 0,\ \Delta J = +2$) we have:

$$\Phi_J = \frac{7(J+1)(J+2)}{30(2J+3)} \gamma^2 \tag{13}$$

while for anti-Stokes ($\Delta\nu = 0,\ \Delta J = -2$):

$$\Phi_J = \frac{7J(J-1)}{30(2J-1)} \gamma^2 \tag{14}$$

For Stokes ro-vibrational lines of the Q branch ($\Delta\nu = 1,\ \Delta J = 0$):

$$\Phi_J = \frac{b_\nu^2(2J+1)}{[1-exp(-hc\tilde{\nu}_{vib}/k_BT)]}\left[a'^2 + \frac{7J(J+1)}{45(2J+3)(2J-1)}\gamma'^2\right] \tag{15}$$

for Stokes ro-vibrational lines of the O branch ($\Delta\nu = 1,\ \Delta J = -2$):

$$\Phi_J = \frac{b_\nu^2}{[1-exp(-hc\tilde{\nu}_{vib}/k_BT)]}\frac{7J(J-1)}{30(2J-1)}\gamma'^2 \tag{16}$$

and finally for Stokes ro-vibrational lines of the S branch ($\Delta\nu = 1,\ \Delta J = +2$):

$$\Phi_J = \frac{b_\nu^2}{[1-exp(-hc\tilde{\nu}_{vib}/k_BT)]}\frac{7(J+1)(J+2)}{30(2J+3)}\gamma'^2 \tag{17}$$

where:

$$b_\nu^2 = \frac{h}{8\pi^2 c\tilde{\nu}_{vib}} \tag{18}$$

The molecular constants a'^2, γ^2, and γ'^2 needed for the calculation of Raman scattering cross sections of molecular nitrogen and oxygen are listed in Table 1.

1.1.3.2 **Carbon dioxide**

For more complex molecules, experimental data is better suited for the simulation of Raman spectra. Carbon dioxide differential cross sections were calculated with the following equation [27, 28]:

$$\frac{d\sigma}{d\Omega} = \left(\frac{\pi}{\epsilon_0}\right)^2 (\tilde{\nu}_0 + \Delta\tilde{\nu})^4 \frac{gM^2}{Q(T)} \exp\left[-\frac{hc\tilde{\nu}_i}{k_B T}\right] \tag{19}$$

where the experimental values for the Raman shift $\Delta\tilde{\nu}$ expressed as wavenumber, the energies $\tilde{\nu}_i$ of the initial state, the vibrational degeneracy g of the transition, and the transition moments M for the four most intense Raman lines are listed in Table 3. These lines can be found in the range 371-374 nm for an excitation wavelength of 354.7 nm.

Table 3: Constants for the calculation of the four most intense carbon dioxide Raman transitions [27].

$\Delta\tilde{\nu}$ [cm^{-1}]	1285.4	1388.2	1265.1	1409.5
M [10^{-42} CV^{-1} m^2]	5.587	6.799	5.44	7.26
$\tilde{\nu}_i$ [cm^{-1}]	0.0	0.0	667.4	667.4
g	1	1	2	2

It is worth to note that experimental cross sections are often obtained, as in this case, by measuring the value in a direction perpendicular to the polarization direction of linearly polarized incident light. In this geometrical configuration, Equation 19 is independent of the scattering angle, and thus is valid for the differential backscattering cross section [29].

The partition function $Q(T)$ is estimated with a polynomial fit of the values from [30] in the 180-300 K range:

$$\mathrm{Q}(T) = 1.059254 \cdot 10^{0} - 8.341959 \cdot 10^{-4} \cdot T + 3.107028 \cdot 10^{-6} \cdot T^{2} \quad (20)$$

1.1.3.3 **Water vapor**

Water vapor Raman cross sections were calculated in the O-H stretching region (3100-4300 cm^{-1}, corresponding to the range 398-419 nm for an excitation wavelength of 354.7 nm). As for CO_2, the differential cross sections were calculated from experimental data using Equation 19, with coefficients

$$\mathrm{A} = \left(\frac{\pi}{\epsilon_0}\right)^2 \cdot gM^2 \quad (21)$$

from [31] and the partition function calculated with a polynomial fit of the values from [32] in the 175-325 K range:

$$\mathrm{Q(T)} = -1.355703 \cdot 10^{1} + 3.871689 \cdot 10^{-1} \cdot T + 8.365774 \cdot 10^{-4} \cdot T^{2} \quad (22)$$

1.1.4 Line broadening

All previous calculations assume infinitely narrow emission lines. In reality multiple effects contribute to the broadening of those lines. Among others, the relevant effects for a Raman lidar are the broadening due to the spectral distribution of the laser-emitted radiation (as the laser wavelength is not perfectly monochromatic), Doppler broadening, and pressure broadening. The overall effect is the convolution of the different profiles.

Multimode Nd:YAG lasers have Gaussian gain profiles with FWHM in the order of 1 cm^{-1}. Single longitudinal mode Nd:YAG lasers, as the one used for the CO_2 measurements presented in this thesis, have line shapes with typical FWHM of around 0.005 cm^{-1} [33–35].

Doppler broadening arises from the thermal motion of the scatterers, leading to a Gaussian spectrum with FWHM depending on the gas temperature. At 300 K and 370 nm the FWHM for oxygen molecules is around 0.12 cm^{-1} [26].

Finally, pressure (or collisional) broadening is due to the collision of other molecules with the scatterer. This effect depends on both the density and the temperature of the gas, with a typical FWHM at 1 atm and 300 K of around 0.05 cm^{-1} [36]. The broadening effect is described by a Lorentzian profile:

$$f(\tilde{\nu}) = \frac{1}{\pi} \frac{\gamma(p,T)}{(\tilde{\nu}-\tilde{\nu}_{\mathrm{Raman}})^2+\gamma^2(p,T)} \tag{23}$$

$$\gamma(\mathrm{p},\mathrm{T}) = \gamma_{air} \left(\frac{p(z)}{p_0}\right) \left(\frac{T_0}{T(z)}\right)^{n_{air}} \tag{24}$$

where $\tilde{\nu}_{Raman}$ is the wavenumber of the unbroadened Raman line, γ_{air} is the air-broadened HWHM at $T_0 = 300$ K and reference pressure $p_0 = 1$ atm, and n_{air} is the coefficient of the temperature dependence of the air-broadened half width.

Due to the interest in the quantification of the contribution of the O_2 ro-vibrational spectrum tails to the CO_2 Raman signal, pressure broadening was modelized and added as an option to the simulator. Laser line shape and Doppler broadening contributions were neglected as at sea-level pressure broadening is the major contributor to the tails of the line shapes.

The backscattering cross section at wavelength λ and in an interval of width Δλ can be calculated as:

$$\frac{d\sigma}{d\Omega}(\lambda) = \sum_i f_i(\lambda) \frac{d\sigma_i}{d\Omega} \Delta\lambda \tag{25}$$

with a sum extended over all the simulated Raman lines.

1.2 Background estimation

Under daylight conditions, the receiving telescope, in addition to collecting atmospheric echoes stimulated by the laser radiation, also detects radiation emitted by the sun. This radiation, incidentally entering the telescope field of view, is an additional source of noise for the lidar measurements, leading to an increase of the corresponding statistical

uncertaninty. Since this undesired signal may have an amplitude comparable to the lidar echoes, it has to be properly modeled.

Two different methods were adopted for the computation of the background signal. Preliminary CO_2 simulations (Chapter 2) were performed using the single scattering approximation. When a more accurate estimation of the background was needed (for example for the calibration of the CO_2 mixing ratio profiles, see Section 6.1), a comprehensive radiative transfer model was used.

1.2.1 Single scattering approximation

In single scattering approximation the background signal is obtained by integrating the contribution of the solar radiation scattered by the atmospheric constituents along the vertical path [37]:

$$B(\lambda) = S_0(\lambda)\Delta\lambda \cdot \tau(\lambda)\epsilon(\lambda) \cdot A\pi(\mathrm{FOV})^2 \int_{z_0}^{z_{TOA}} \left[\beta_{mol}(\lambda, z)\frac{P_{Ray}(\theta)}{P_{Ray}(\pi)} + \beta_{aer}(\lambda, z)\frac{P_{HG}(\theta)}{P_{HG}(\pi)}\right] T_{sun}(\lambda, z)T(\lambda, z)\mathrm{d}z \quad (26)$$

where S_0 is the solar spectral irradiance (considered values are from the ASTM G173 Reference spectrum [38]), θ is the scattering angle, which for a ground-based lidar pointing at the zenith is equal to the sun zenith angle. FOV is half the telescope field of view (half width half maximum - HWHM), T_{sun} is the transmittance from the top of the atmosphere (TOA) to the scattering volume at height z and T is the transmittance from z to z_0. The scattering coefficients at the angle θ are obtained from the backscatter coefficients β_{mol} and $\beta_{aer}(\theta = \pi)$ using the Rayleigh phase function [19]:

$$P_{Ray}(\theta) = \frac{3}{16\pi}(1 + \cos^2\theta) \quad (27)$$

and the Henyey-Greenstein approximation [39]:

$$P_{HG}(\theta) = \frac{1}{4\pi}\frac{1-g^2}{(1+g^2-2g\cos\theta)^{3/2}} \quad (28)$$

where the asymmetry parameter was set to $g = 0.987$.

1.2.2 SCIATRAN

SCIATRAN [40–42] is a highly consolidated open-source software that can simulate radiative transfer processes, including multiple scattering and polarization through Earth's atmosphere for different observation and illumination geometries. The software package can perform fast and accurate simulations of radiance spectra appropriate to atmospheric remote-sensing observations in a spectral range going from the ultraviolet (UV) to thermal infrared (TIR). Different models and databases are included in SCIATRAN, and various gaseous absorbers are taken into account.

These features make the software a perfect candidate for the calculation of zenith radiance and background signal for a ground-based lidar.

The following input parameters were used in the simulations:

- pseudo-spherical atmosphere (for solar zenith angles up to ~92°)
- vector discrete ordinate technique (the RTM includes polarization effects)
- solar spectrum: MODTRAN3.7 [43]
- molecular scattering: Bodhaine, 1999 [20]
- spectral segments 371.0-372.5 and 385.5-388.0 nm at 0.01 nm resolution
- gas absorption: BRO, NO_3, OCLO, O_4, O_3, NO_2, SO_2, ClO, HCHO, O_2, H_2O, CO_2, N_2O, CO, CH_4, NO, NH_3, HNO_3, OH, HF, HCL, HBR, HI
- surface albedo: 0.2
- height above sea level: 800 m
- aerosol parameterization type: Aeronet (340, 380, 440 and 500 nm aerosol optical thickness, phase function and vertical distribution) [44]
- sun zenith angle and the relative azimuth calculated using the NOAA Solar Calculator [45]

2 Preliminary CO_2 simulations

Preliminary simulations were performed in order to evaluate the possibility of exploiting one or both Raman lines of the CO_2 ν_1:$2\nu_2$ Fermi resonance [46]. As some ro-vibrational O_2 lines lie in the same spectral range and represent a potential source of contamination for CO_2 measurements, an accurate evaluation and quantification of this disturbance source has been carried out. Thus, the optimal position and width of the filter for the measurement of the Raman backscattering from CO_2 was defined. The signal integration over the vertical and over time required to reach a useful signal to noise ratio both in day-time and night-time needed for a quantitative analysis of carbon dioxide sources and sinks was evaluated. Finally, the capability to estimate variability of the CO_2 mixing ratio was assessed.

The above objectives were obtained developing an instrument simulator code (Section 1) consisting of a RTM able to simulate, in a spectrally resolved manner, all relevant laser light interaction mechanisms with atmospheric constituents, a consistent background signal, and all the characteristics of the considered Raman lidar experimental setup.

The lidar simulator was used to simulate O_2 and N_2 ro-vibrational spectrum and the first four more intense CO_2 Raman lines, among which the Fermi doublet at 1285.4 cm^{-1} and 1388.2 cm^{-1}, or 371.69 nm and 373.11 nm for an excitation wavelength of 354.74 nm. Pressure broadening (that is, Lorentzian broadening) was applied for a rough estimation of the impact of the tails of the O_2 broadened lines on the CO_2 measurements at low altitudes. A fixed value of γ_{air} = 0.05 cm^{-1} was used for the Lorentzian function FWHM, with a temperature coefficient $n_{air} = 0.7$. A fixed value of x_{CO2}=415 ppm was used for the CO_2 concentration. Aerosol extinction was computed with a parametrized representation based on: aerosol optical thickness $\tau_{380} = 0.2$, Angstrom exponent AE = 1.5 and a scale height h = 2 km, having assumed that the aerosol concentration decreases exponentially. Solar background was calculated at 371.7 nm and 386.7 nm in single scattering approximation for different solar zenithal angles. The uncertainty assumes Poissonian statistics of the received photon counting signal.

The simulations were based on preliminary characteristics of the CONCERNING lidar:

- monochromatic laser source at $\lambda_0 = 354.74$ nm
- single pulse energy $E_0 = 0.1$ J
- repetition rate $f = 100$ Hz
- optical transmission efficiency of η = 0.90
- detector quantum efficiency of ϵ = 0.43
- CO_2 interference filter with peak transmission τ = 0.46, FWHM of 0.15 nm, theoretical spectral shape provided by the manufacturer Materion

- N_2 interference filter with peak transmission of τ = 0.8, FWHM of 0.3 nm, theoretical spectral shape provided by the manufacturer Alluxa
- telescope radius of 0.25 m with a FOV (full angle) of 0.1 mrad

Further assumptions were:

- lidar altitude of 0 m a.s.l.
- 1976 U.S. Standard Atmosphere [24]
- full overlap assumed for the whole atmosphere

First, the whole spectrum (350-410 nm) was simulated with a 0.0001 nm resolution in order to quantify the effect of the tails of the broadened O_2 and N_2 lines on the CO_2 measurements. Figure 3 shows the simulated spectrum (at 1013 hPa and 288 K), including the CO_2 Raman lines of interest, together with the transmittance of two filters centered at 371.69 nm (filter A) and 373.11 nm (filter B).

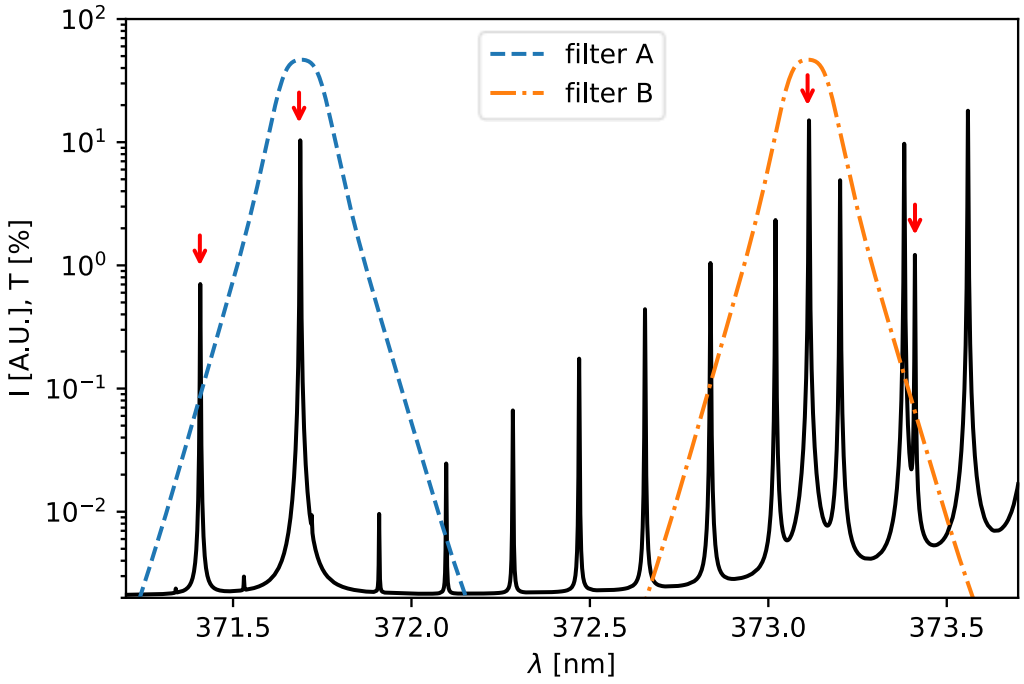

Figure 3: Simulated Raman spectrum (solid line) and filter transmittance T for filter A (dashed) and filter B (dash-dotted). The CO_2 Raman lines are indicated by the arrows, the remaining lines are O_2 ro-vibrational lines. The underlying "background" signal is the result of the broadening of all the calculated lines.

The simulations indicate that the broadened Raman signal due to the lines' tails, integrated over the filter A window, has low intensity but still could be not negligible. It can account for up to 1% of the total signal under simulated conditions, potentially leading to systematic errors of up to 4 ppm in the retrieved mixing ratios. It should be noted that the calculated value is expected to be an overestimation of the real Raman tail contribution. Furthermore, this component of the signal is expected to diminish at lower pressures and temperatures, where the Doppler broadening dominates. The

simulation should be performed with a more accurate broadening model and coefficients. Nevertheless, due to the difficulty in modelling the broadened tails at several nanometers from the broadened Raman lines, in order to have accurate measurements at sea-level this contribution to the signal should be better investigated experimentally with measurements slightly below 371 nm (for example, with the same filter shifted in frequency with angle tuning or with a scanning spectrometer).

The second step was the evaluation of the impact of the unbroadened O_2 lines falling inside the filter transmission ranges. The simulation confirms the calculations done by [12], with the 21st O_2 ro-vibrational line contributing with less than 0.1 % to the Filter A signal (corresponding to less than 1 ppm systematic error). The O_2 contribution on filter B signal is instead in the order of 10-15%.

Further narrowing of the interference filters or an accurate estimation of the temperature dependency of the lines would be necessary to take advantage of the 373.1 nm line (filter B). Still, line modeling paired with simultaneous temperature measurements should lead to an uncertainty on the filter B-retrieved mixing ratio of less than 1 ppm/K (see Figure 4), with a dependency on the uncertainty of the temperature profile.

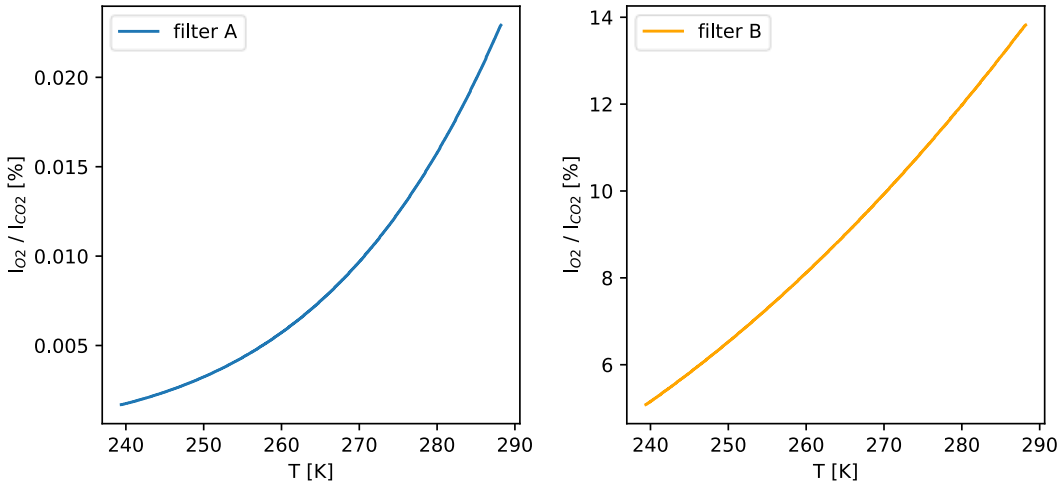

Figure 4: Temperature dependence of the contribution of the O_2 lines relative to the CO_2 signal for Filter A (left) and Filter B (right).

As a third step, the temporal integration necessary to reach a given statistical uncertainty using filter A during night-time and day-time was calculated. Assuming Poissonian statistics for the lidar signals, the time needed to reach the uncertainty Δx_{CO2} was calculated as:

$$t = \frac{{x_{CO2}}^2}{f\,{\Delta x_{CO2}}^2}\left(\frac{P_{CO_2}+B_{CO_2}}{P_{CO_2}^2}+\frac{P_{N_2}+B_{N_2}}{P_{N_2}^2}\right) \tag{29}$$

where f is the repetition rate of the lidar system and x_{CO2} is the CO_2 mixing ratio.

The integration time *t* needed to reach at a given altitude *z* the required measurement precisions (1 ppm, 5 ppm) was calculated in different background conditions (night, SZA=60°, SZA=30°) and for different vertical resolutions (7.5 m, 75 m, 300 m). The results (see Figure 5) indicate that the simulated lidar system could perform measurements on the low troposphere gradients with good precision (1 ppm) both in day-time and night-time with an integration time of 1-3 h.

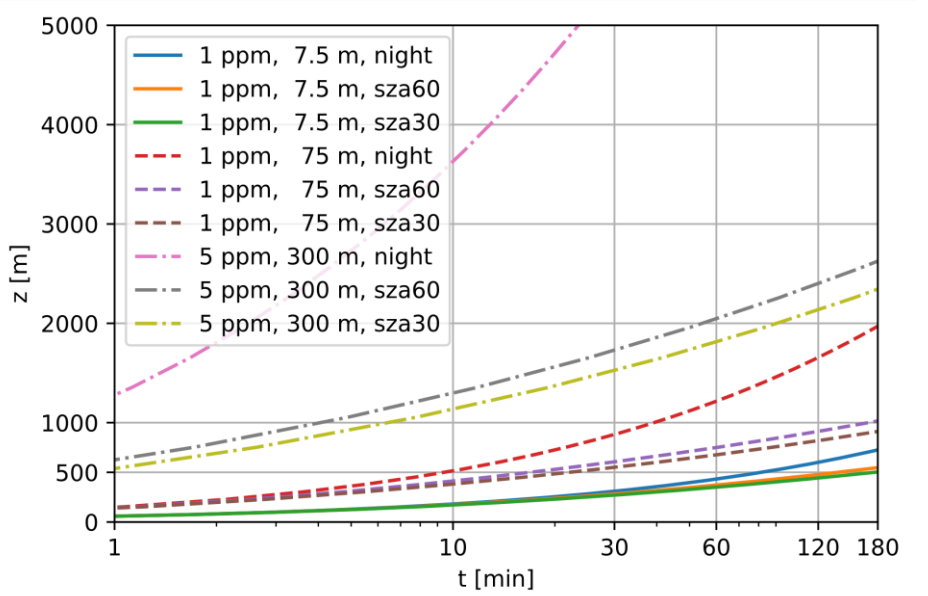

Figure 5: Integration time t required to reach a given altitude z for different background conditions (night, SZA=60°, SZA=30°), vertical resolutions (7.5 m, 75 m, 300 m) and measurement precisions (1 ppm, 5 ppm).

These preliminary results confirmed that a state-of-the-art Raman lidar system dedicated to the measurements of CO_2 profiles could perform measurements in the low troposphere with sufficient precision to estimate gradients due to carbon sources and sinks. Both considered Raman lines could be used and the signal contamination attributed to the O_2 ro-vibrational Raman lines could be mitigated via line modeling. Being the simplest and more robust solution, a configuration with a single filter centered at 371.69 nm was selected for the CO_2 Raman channel of the CONCERNING lidar.

Further analysis should include a more accurate theoretical or experimental estimation of the signal contamination due to line broadening and the estimation of the uncertainty for different aerosol types and atmospheric profiles.

These simulations were based on a preliminary setup and some differences can be found between the simulated and actual characteristics of the CONCERNING lidar. Among the others, a larger field stop resulted in lower performances during daytime due to the higher background. Night-time performances instead are not far (0.63 times less photoelectrons per range bin) from the simulated results and are only slightly affected by these differences (see Figure 6).

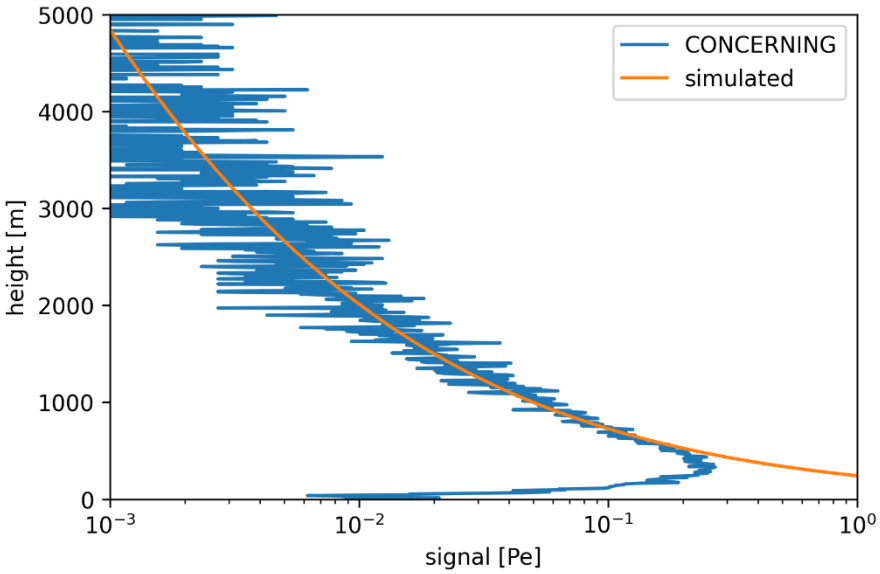

Figure 6: Measured (1-minute average) and simulated single shot CO_2 signal with 7.5 m vertical resolution, a scaling factor of 0.63 was applied to the simulated data.

3 Instrument development

The two lightweight, compact ground-based systems here described are designed to precisely measure a variety of atmospheric parameters with high temporal and spatial resolution, enabling the resolution of convection scales and turbulent processes. These systems utilize both rotational and vibrational Raman lidar techniques in the UV spectrum, employing advanced technologies for laser emission, spectral selection, optical signal detection, and data acquisition. Housed in sealed, rugged containers with fused-silica windows, they are capable of operating in all weather conditions and can be remotely operated with 24/7 measurement capabilities.

The two instruments were developed in 2022, and after a brief period of test deployed in a variety of national and international measurement campaigns, demonstrating their measurement capabilities and the potential impact of such systems.

3.1 CONCERNING

CONCERNING (COmpact RamaN lidar for Atmospheric CO_2 and ThERmodyNamic ProfilING) [47] is a Raman lidar that can operate at three wavelengths (354.7, 532.1 and 1064.2 nm) and potentially equipped with twelve channels, eight of these currently fully operational: three elastic signals at 354.7 nm (total, parallel, and cross polarized with respect to the polarization of the laser radiation), the ro-vibrational N_2 , H_2O, and CO_2 Raman signals and the rotational Raman $N_2 - O_2$ signals at low and high quantum number J. All the operational channels are stimulated by the 3rd harmonic of the laser emitter (353.7 nm). Other four potential channels taking advantage of the other two emitted wavelengths can detect the total and parallel elastic signals at 532 nm, the total elastic signal at 1064 nm, and the ro-vibrational N_2 signal at 607.4 nm.

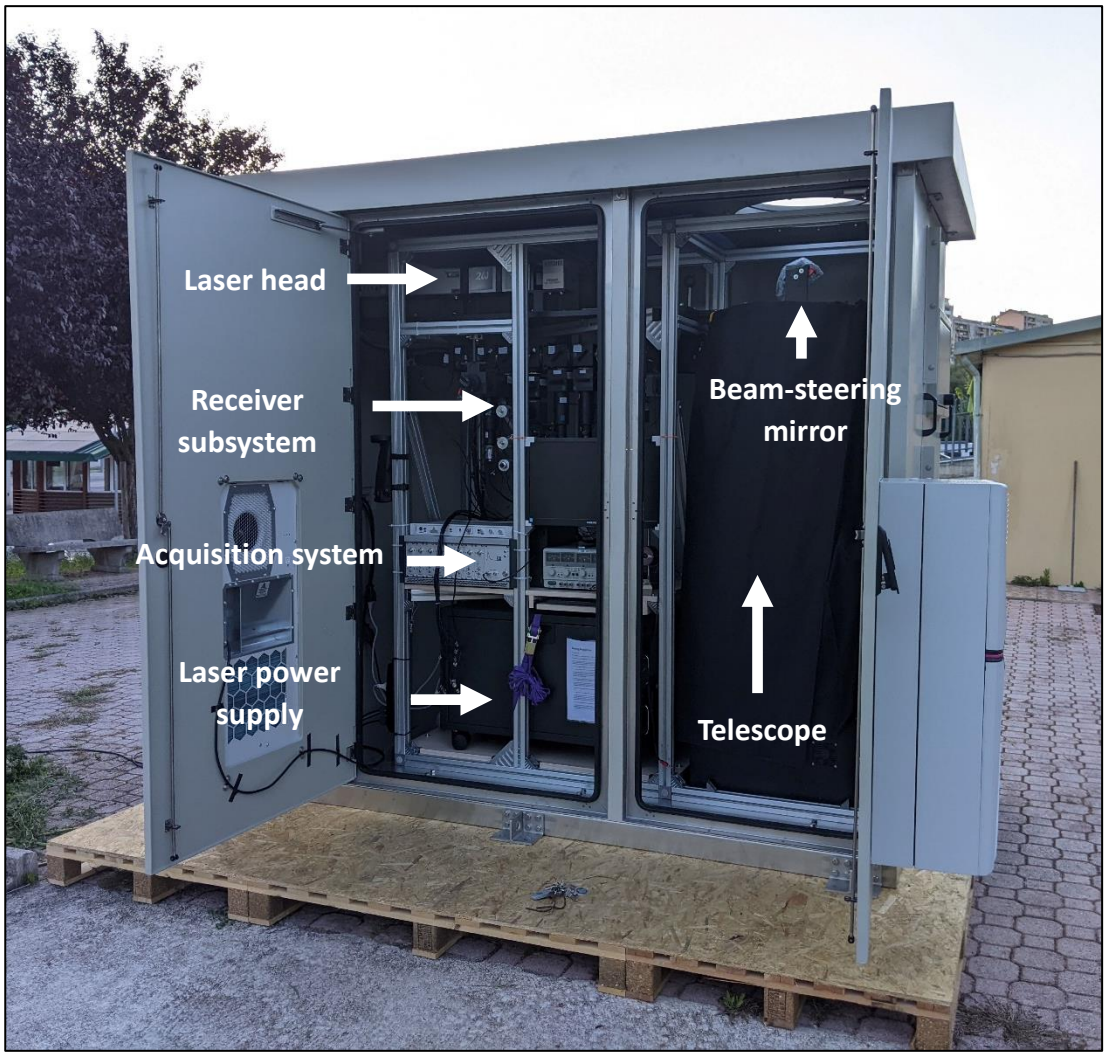

Figure 7: Internal view of the CONCERNING lidar system.

The laser source, a customized version of Merion MW 7-100 produced by Lumibird, is a water-cooled diode-pumped Nd:YAG with a master oscillator-power amplifier configuration. It has high frequency stability (< 5 pm) and narrow laser line (< 0.005 cm^{-1} FWHM). These properties are obtained through injection seeding through a diode laser. The single pulse energy is 110 mJ at 355 nm, which at a repetition rate of 100 Hz gives an average power of 11 W. The beam diameter is around 6.5 mm at the laser head exit. The laser head is water cooled through the use of a chilling unit (integrated with the power supply), which in turn is cooled with a secondary circuit using tap water or a chiller placed outside the lidar (as done during the WaLiNeAs campaign, described in Sect. 5.1). The laser characteristics are listed in Table 4. After the second and third harmonic crystals, the residual visible and infrared beams are separated from the UV beam using dichroic mirrors and dumped. Both the dichroic assembly and the dumper are optional and can be removed for multiwavelength operation. The laser beam is then expanded by a reflective 6x beam expander produced by Trioptics (BEX 6.5/39). The off-axis design of the beam expander (off-axis paraboloid + spherical mirror) produces no central obstruction and the use of the achromatic reflective configuration permits the

operation from UV to IR without adjustments. The expansion reduces the beam divergence from 0.39 mrad to 65 µrad (measured value ≤ 120 µrad). The laser is then deflected vertically, in a coaxial lidar configuration, by a 3" motorized beam-steering mirror (UV enhanced aluminium coating) that can be controlled by a computer, allowing for boresight alignments, that is, the co-alignment of the laser beam and the telescope field of view.

Table 4: Technical specification of the CONCERNING laser source.

Laser type	Seeded Nd:YAG (diode-pumped)
Wavelength [nm]	354.74, 532.11 and 1064.22
Linewidth @ 1064 nm [cm^{-1}]	<0.005
Nominal energy / power @ 355 nm	110 mJ (11 W)
Pulse to pulse energy stability @ 355 nm	1.3% RMS
Power drift @ 355 nm	< 1%
Rep. rate [Hz]	100
Pulse width [ns]	6
Beam diameter [mm]	6.5
Pointing stability [µrad]	6
Beam divergence, full angle [mrad]	0.39
Polarization ratio/Direction @1064 nm	98% Vertical
Warm-up time [minutes]	<20
Cooling method	Water to water
Oper. envir. temp. [°C]	18–28
Power requirements	Power supply: 220 V, ~7.5 A Cooling group: 220 V, ~10 A

The system operates in eye-safety conditions only from a certain distance. UV eye-safety threshold at 355 nm, computed in compliance with the International Standard IEC 60825-1:2014 [48], for exposure times from 1 ns up to 10 s, is quantified as the maximum permissible exposure (MPE) through the empirical formula $MPE = 5.6 \times 10^3 \times t^{0.25}$ J m^{-2}. For an exposure time of 6 ns (single pulse), and considering the nominal divergence (65 µrad) and diameter (39 mm) after the beam expander, eye-safety is achieved from an altitude of approximately 220 m. Exposure times up to 1 s lead to similar nominal ocular hazard distances (NOHD), and the system, although not eye-safe at the exit aperture, should be considered safe for aviation.

The backscattered signal is then collected by a Newtonian telescope produced by Explore Scientific (20” Ultra Light Dobsonian Gen II) with aluminium open truss tube design. The primary mirror is a 500 mm diameter parabolic mirror with 94% reflectivity aluminium coating, and focal length of 1800 mm, giving an f-number of f/3.6. The secondary mirror produces an obstruction of 120 mm diameter. The technical specifications of the telescope and other CONCERNING lidar characteristics are listed in Table 6.

The focused beam passes through a 1 mm diameter field stop, is then recollimated and sent for the wavelength separation. The optical layout includes several beam splitters and dichroics (producer: Eksma Optics) chosen to efficiently divide the collected signal (Figure 8). For the spectral selection, interference filters with narrow bandwidths (0.15-0.5 nm) and high out of band rejection produced by Alluxa and Materion are used. In its initial configuration, the receiver included seven receiving channels: the total, co- and cross-polarized elastic backscatter signals at 354.7 nm, the ro-vibrational Raman backscatter signal by N_2 molecules at 386.7 nm, the ro-vibrational Raman backscatter signal by H_2O at 407.5 nm, and the LoJ and HiJ rotational Raman channels at 354.3 and 352.9 nm, respectively. The CO_2 Raman channel at 371.7 nm was added and tested in late 2023 and is now part of the operational configuration. Spectral specifications can be found in Table 5.

Table 5: Spectral specifications of the CONCERNING interference filters. CW stands for filter center wavelength, BW stands for filter bandwidths.

Reception channels	CW [nm]	BW [nm]	Peak Trans. [%]	Blocking
Elastic total	354.7	0.5	80	≥OD7
Elastic par. polarized	354.7	0.5	80	≥OD7
Elastic perp. polarized	354.7	0.5	80	≥OD7
N_2 ro-vib. Raman	386.7	0.3	80	≥OD7
H_2O ro-vib. Raman	407.5	0.3	80	≥OD6
CO_2 vibrational Raman	371.7	0.15	60	≥OD6
Rotational Raman LoJ	354.3	0.3	80	≥OD6
Rotational Raman HiJ	352.9	0.5	80	≥OD6

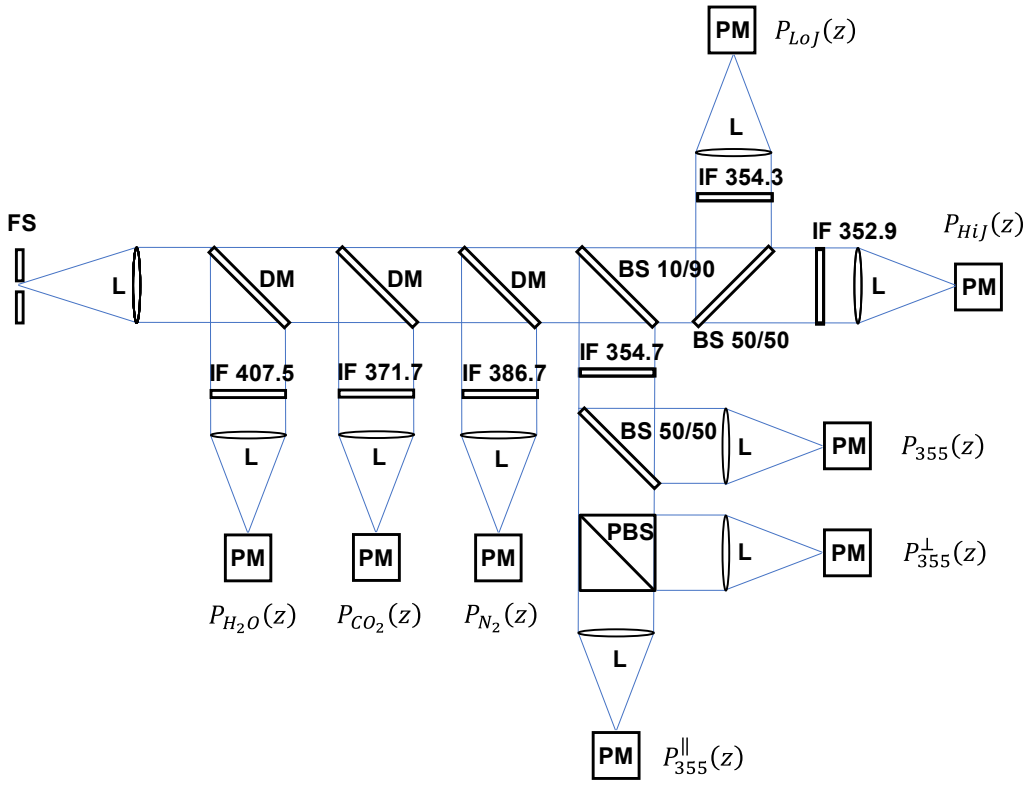

Figure 8: Block diagram of the current CONCERNING optical setup. PM: photo-detection modules, L: lens or refractive collimating system, DM: dichroic mirror, BS: beam splitter, IF: interference filter.

The signal detection is performed by photomultiplier tube (PMT) modules with low dark count optimized for photon counting measurements, high quantum efficiency (43% peak quantum efficiency in the UV), and high gain (≈10^6) produced by Hamamatsu (H10721P-210). These photosensor modules contain a metal package PMT and a high-voltage internal power supply circuit that can be powered by a low voltage 5 V external power supply. Raman lidar signals are inherently weak, and during the daytime, they can become significantly weaker than the solar background radiation. At night, when solar radiation is absent and environmental background noise is minimal, these weak lidar signals can be effectively sampled using photo-counting mode. However, during the day, with strong solar background, photo-counting becomes ineffective. This is because photons from Raman echoes combine with those from solar radiation, resulting in a signal that exceeds the count rate suitable for photo-counting. In such cases, analog acquisition of the photoelectron current is preferred. The signal is therefore acquired in both photon-counting (800 MHz) and analog detection (16 bit, 40MHz) modes using a transient recorder produced by Licel (TR40-16bit-3U). The acquisition system has pre-trigger measurement capability, that is, the acquired signal consists of 1/16th of the transient recorder memory tracelength before the trigger and the remaining points after the trigger point.

The entire system is located inside an air-conditioned cabinet of 2600 x 1340 x 2265 mm, equipped with a 500 mm fused-silica window with anti-reflection coatings on both sides, which allows to operate in any weather condition. The air conditioners are sized to allow the removal of heat produced inside the cabinet during operation, and the presence of two units guarantees redundancy in case of malfunction. The fiber-glass cabinet can be completely dismantled in order to provide easy access to the lidar system. The window and the roof of the cabinet have a 3-degree slope for optimal rain draining and clearing. A 900 x 900 x 600 mm sunshade keeps direct solar radiation from entering the window at sun zenith angles up to ∼45 degrees, and from hitting the alignment mirror up to ∼35 degrees. The system is transportable and suitable for field campaigns and can be operated remotely, taking measurements 24/7.

Table 6: Lidar CONCERNING characteristics.

Telescope	Newtonian
Focal length [mm]	1800
Primary mirror dia. [mm]	500
f-number	f/3.6
Secondary mirror obs. dia. [mm]	120
Field of view [FWHM, mrad]	0.55
Full overlap [m]	∼800
Detectors: Peak quant. eff. [%] Gain	Photomultiplier tubes 43 $2–4 \times 10^6$
Max. vertical sampling resolution [m]	3.75 (analog and photon counting)
Acquisition system	16 Bit, 40 MHz analog, 800 MHz photon counting

3.2 MARCO

MARCO (Micro-pulse Atmospheric optical Radar for Climate and weather Observations) [47] is a compact and easily transportable Raman lidar system based on a micro-pulse laser source. The name was given in remembrance of Prof. Marco Cacciani, a brilliant lidar scientist and a mentor for a large portion of the Italian lidar community, who passed away in January 2022.

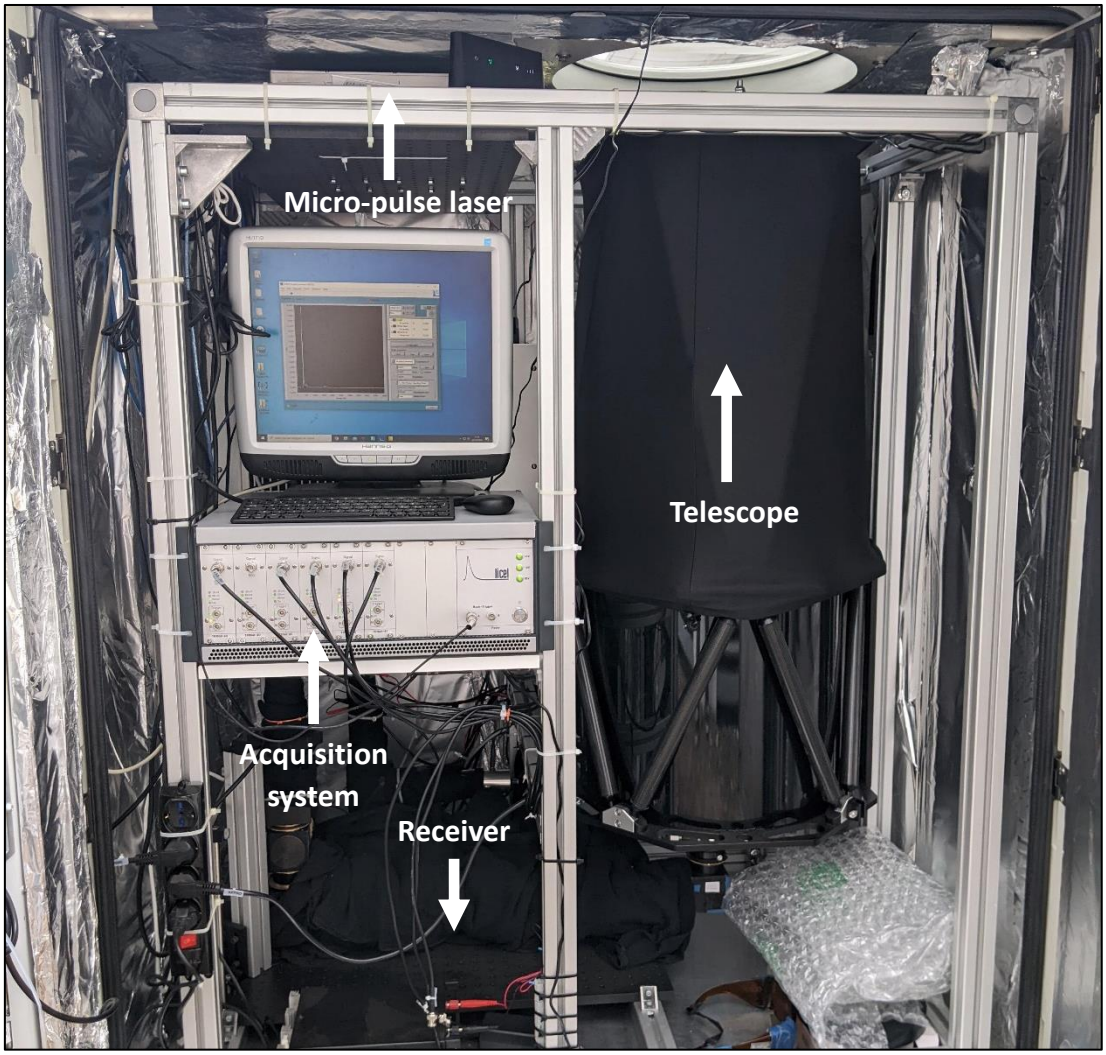

Figure 9: Internal view of the Raman lidar system MARCO. The different major sub-systems are clearly visible in the picture (micro-pule laser, telescope, receiver, acquisition system).

The lidar transmitter has been developed around a high-power UV micro-pulse laser. The micro-pulse source (Sintec Optronics, model STC-AO-V-355-Water) is an all solid state, diode-pumped, Q-switched laser based on acousto-optic modulation (AOM). It operates at 354.7 nm with high peak power, high repetition rate, and short pulse duration. The technical specifications of the laser source are listed in Table 8. The pulse repetition rate can be changed within the interval 10–40 kHz, with different single pulse

energies at the different frequencies. During the measurements reported in this thesis, the laser was operated at a frequency of 20 kHz, with a single pulse energy of 250 μJ and an average emitted power of 5 W (begin of life) at 354.7 nm. This was considered to be the best possible compromise between the system performance and its capability to achieve the scientific goals of the measurement campaigns. A repetition rate of 30 kHz could have been used, which could have led to a larger emitted power (6 W). However, this would lead to the overlap of lidar echoes from successive laser pulses beyond 5 km. The lower repetition rate of 10 kHz, allowing sampling up to 15 km and potentially solving background subtraction issues, has instead been discouraged by the laser manufacturer for long-term use. The average emitted power decreased as expected over nearly one and a half years of continuous use, reaching 2.5 W due to diode degradation.

Table 7: MARCO laser source technical specifications.

Laser type	Nd:YAG
Wavelength [nm]	354.7
Operating mode	Acousto-Optic Q-switched
Average power [W]	1–5 (6 W @ 30 kHz)
Repetition rate [kHz]	10–40
Pulse energy @10 kHz [μJ]	190
Pulse energy @20 kHz [μJ]	250
Pulse energy @30 kHz [μJ]	200
Pulse energy @40 kHz [μJ]	140
Pulse width [ns]	~12 @ 30 kHz
Warm-up time [minutes]	<10
Transverse mode	TEM00
Beam diameter [mm]	8
Beam divergence, full angle [mrad]	<0.3
Beam quality (M^2)	<1.3
Polarization ratio/Direction	>99%, Horizontal
Cooling method	Water cooled
Oper. envir. temp. [°C]	15–35
Power requirements	Laser: 300 W Chiller: 460 W

As system CONCERNING, MARCO operated in eye-safety conditions only from a certain distance. Due to the low energy per pulse, the single-pulse eye-safety requirement is satisfied. However, for an exposure time of 10 s eye-safety was achieved from an altitude of approximately 240 m. Shorter exposure times lead to lower NOHDs, for example $NOHD_{1s}$ = 85 m, $NOHD_{0.1s}$ = 20 m. Therefore, also the system MARCO was not considered eye-safe at the exit aperture, but still safe for aviation. Eye-safety at all distances, including the exit aperture, was achieved in this system through further expansion of the laser beam, as done during the DECIPHER campaign (see Section 5.3).

The laser head is water cooled through the use of a chilling unit, hosted inside the lidar cabinet. The laser head, power supply and chilling unit are very compact, allowing a small overall dimension of the lidar instrument.

The 8 mm diameter UV laser beam is deflected by a 1" 45-degree motorized mirror. Despite the biaxial lidar configuration, the position of the mirror inside the primary mirror footprint contributes to the partial obscuration of the latter.

The receiver has been built around a Ritchey–Chrétien telescope (Omegon, model: 53815-406/3250), with a primary mirror (diameter: 406 mm), a secondary mirror (obstruction diameter: 190 mm), and a combined focal length of 3250 mm. The mechanical structure of the telescope is a carbon-fiber truss-tube. The technical specifications of the telescope are listed in Table 8, together with the specifications of the major receiver sub-systems.

The radiation collected by the telescope passes through a 1 mm field stop. Due to the telescope's longer focal length, this results in a narrower field of view compared to the CONCERNING system, thereby reducing the collected solar background. The collected radiation is divided into different portions entering the different receiving channels through the use of dichroic mirrors and/or beam-splitter plates. In its first configuration, the receiver included five receiving channels: the total, co- and cross-polarized elastic backscatter signals at 354.7 nm, the ro-vibrational Raman backscatter signal by N_2 molecules at 386.7 nm, and the ro-vibrational Raman backscatter signal by H_2O at 407.5 nm. The remaining LoJ and HiJ rotational Raman channels were added for the DECIPHER campaign. A block diagram of the optical layout of the system is illustrated in Figure 10.

Table 8: Lidar MARCO characteristics.

Telescope	Ritchey–Chrétien
Focal length (mm)	3250
Primary mirror dia. (mm)	406
f-number	f/8
Secondary mirror obs. dia. (mm)	190

Field of view (FWHM, mrad)	0.31
Full overlap (m)	~500
Detectors: Quant. eff. @ 355 nm (%) Gain	Photomultiplier tubes 43 2–4 × 10^6
Vertical sampling (m)	15 (analogue and photon counting)
Vertical resolution (m)	15–100
Time resolution (s)	3–60
Acquisition system	16 Bit, 40 MHz analogue acquisition, 800 MHz photon counting

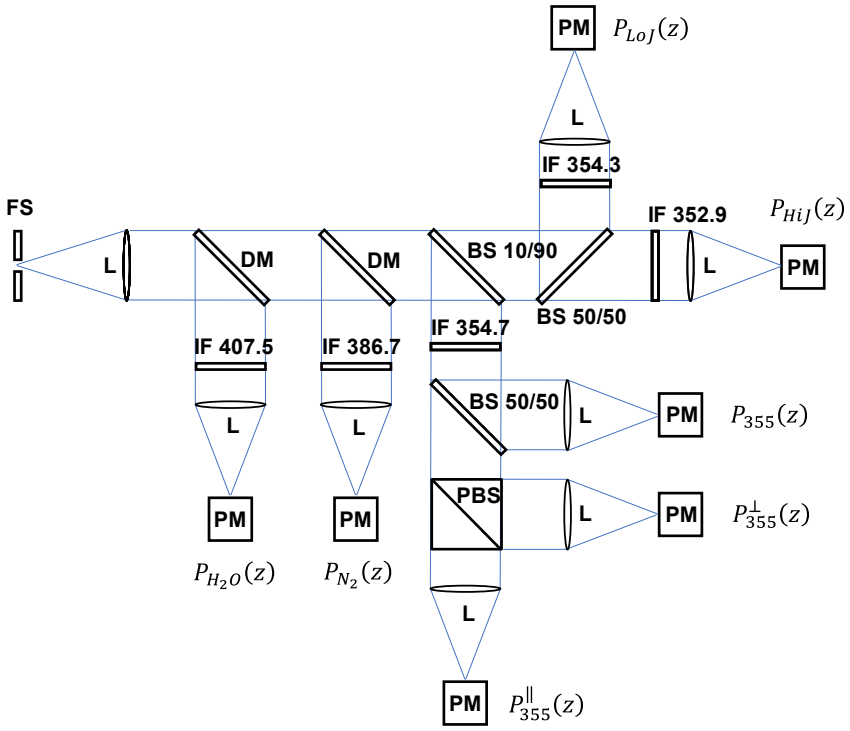

Figure 10: Block diagram of the current MARCO optical setup. PM: photo-detection modules, L: lens or refractive collimating system, DM: dichroic mirror, BS: beam splitter, IF: interference filter.

The receiving system is based on beam splitters, dichroics (producer: Eksma) and interference filters (producer: Alluxa) for the spectral selection. Detection is performed

by Hamamatsu photomultipliers (H10721P-210 and H10721-210), and data acquisition is carried out in both analog and digital mode using Licel transient recorders.

The power consumption of the different subsystems (laser head: 300 W, laser chiller: 460 W, detectors, acquisition system and controlling computer: 100 W) results in an overall power supply requirement not exceeding 900 W.

MARCO is hosted in a small cabinet approximately 1350 x 1200 x 1730 mm, with similar technical characteristics of the one hosting CONCERNING, and a single air conditioner employed in the regulation of the internal temperature. The overall smaller volume, weight and power consumption translates into the possibility to sensitively simplify the logistics and costs associated with the transportation and deployment of the system.

3.3 Prototype development, procedures and issues

Both lidar prototypes were developed, assembled (Figure 11) and tested in 2022 at the Lidar Laboratory of the School of Engineering – University of Basilicata. A list of subsystem procedures, encountered issues, and proposed solutions is here detailed.

Figure 11: CONCERNING lidar prototype during assembly and initial testing in the Lidar Laboratory.

3.3.1 Telescope collimation

Lidar systems act as “light buckets” and, when equipped with relatively large field stops, they are quite tolerant with respect to optical aberrations. The two lidar telescopes were collimated using a standard procedure from amateur astronomy telescopes, which

involves visually aligning the primary and secondary mirrors. While this method is straightforward and practical for disassembled systems, it can become challenging in fully assembled systems. In deployable systems, the telescope can lose collimation during transportation, requiring a recollimation. This is feasible in the CONCERNING lidar, as the telescope and receiver can be easily decoupled for inspection. However, in the MARCO system, the two components are difficult to separate in the field and the telescope difficult to inspect, so alternative collimation methods, such as using a laser collimator embedded in the system, should be developed. As a partial solution, the position of the collimation screws was marked and their position was corrected after transportation, no methods were adopted to check the actual collimation.

3.3.2 Beam expander focus adjustment

The CONCERNING reflective beam expander has a fixed focus and needs no adjustments. Still, a different refractive model (Edmund optics, model: 39-727 5x UV-VIS), with adjustable focus, was used in some preliminary tests. The same beam expander is now being tested in the MARCO lidar system.

In order to collimate the beam, its diameter was measured at different distances from the beam expander: after the beam expander ("zero"), at 2.5 m ("near") and at 8 m ("far"), see Figure 12. Collimation is achieved when all three measurements coincide and the resulting divergence should be less than the diameter measurement precision (1 mm) divided by the distance. The divergence was therefore estimated to be less than 0.12 mrad, the same also applies to the reflective beam expander.

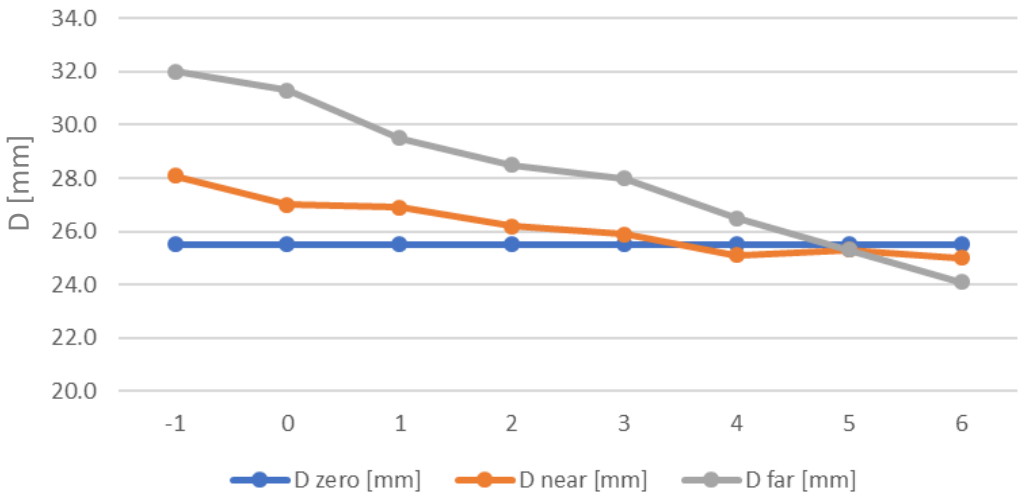

Figure 12: Beam diameter measured at different distances and collimator focus positions (on the x axis).

The short distances, combined with the errors in the beam diameter measurement, limit the precision of the beam divergence estimation. Future lidar prototypes should include an opening in the cabinet permitting the measurement (and adjustment) of the expanded beam in the field at greater distances, in order to achieve better precision in the divergence measurements.

3.3.3 Spurious signals

The signal acquisition subsystem comprising transient recorders, photomultipliers, and their power supplies, as implemented in the two lidar prototypes has been found to be sensitive to electromagnetic interference and other sources of spurious signals. Several sources of signal contamination have been noted in both analog and photon counting modes. High frequency electromagnetic sources from cellphone towers or the laser power supply are mostly detected in the photon counting mode. Signals coming from the laser via ground loops or the trigger cable instead are low frequency distortions mostly captured in the analog mode. To minimize the problem, various solutions have been adopted, such as separating the ground of the various subsystems and partial shielding with aluminum foil and iron plates. In such compact systems, enclosing the entire acquisition subsystem in a Faraday cage is highly recommended and envisioned as a future upgrade; a further solution is the decoupling of the laser and acquisition subsystems by means of an optical trigger.

External electromagnetic interferences result in a higher background signal and consequently a degraded SNR. Raising the photon counting thresholds greatly reduces the number of spurious counts, from both internal and external sources, but at the expense of the real photoelectron count. After minimizing these noise sources with hardware solutions, the low frequency laser-induced spurious signal can also be reduced in the analog channels by dark signal subtraction (see Section 4.1.1).

3.3.4 Thermo-mechanical stability

The nominal temperature variability in the cabinet, expected in the range of 1 degree, turned out to be unrealistic, being this maintained only in limited ranges of external temperature and solar radiation (see Figure 13). Temperature gradients between the lower and upper part of the cabinet were also detected. Finally, the solar radiation entering the window is suspected to be the cause of the instability in the relative geometry between emission and reception, with consequent instability in the collected lidar signals. Internal fans were positioned to homogenize the temperature gradients and distribute the cold air emitted in a discontinuous way by the air conditioners. A larger sunshade is also planned for the next measurement campaigns in order to decrease the solar radiation incident on the window.

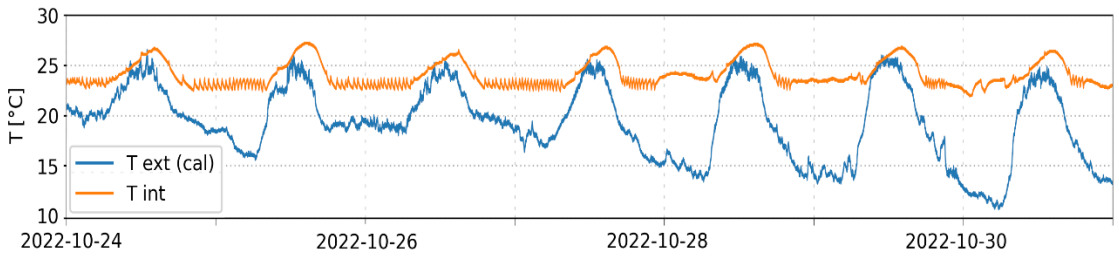

Figure 13: external (blue) and internal (orange) temperatures for the system CONCERNING measured during the WaLiNeAs campaign.

3.3.5 Dirt accumulation

The two systems have demonstrated their remote and automatic measurement capabilities (see measurement campaigns, Section 5), but the absence of personnel on site has proved problematic due to the impossibility of continuous maintenance. The performance of the systems has in fact suffered from the accumulation of dirt on the quartz window due to dust, leaves and insects strongly attracted by the emitted UV radiation. The inclination of the window proved to be sufficient but not optimal, as after rain some dirt accumulates in the lower part. Furthermore, since light rain can deposit additional dust and strong rain events are an unreliable form of cleaning, an automated cleaning system is being evaluated for future developments.

Figure 14: Dirt accumulation on the window of the lidar MARCO during WaLiNeAs campaign.

4 Retrieval algorithms

In the following sections the steps followed for the retrieval of CO_2 mixing ratio, WV mixing ratio, temperature and aerosol backscatter coefficient are detailed. The pre-processing steps are common for all the retrieval algorithms and are applied sequentially to photon-counting and analog channels.

4.1 Pre-processing

4.1.1 Dark subtraction

Dark measurements are acquired with the laser turned on and a shutter or other means to block incoming light from reaching the receiver optics and photomultipliers. These measurements are averaged over 15-30 minutes and subtracted from the signal in order to remove low frequency electromagnetic interferences synchronized with the laser shots (see also Sect. 3.3.3).

Figure 15 shows an example of dark measurement of an analog channel of the MARCO system. The first spike is coincident with the laser pulse, the second with the voltage drop at the end of the trigger pulse, other small ripples come from the diode lamps flashing at 90 kHz. This kind of spurious signals can be partially removed via dark subtraction in analog channels.

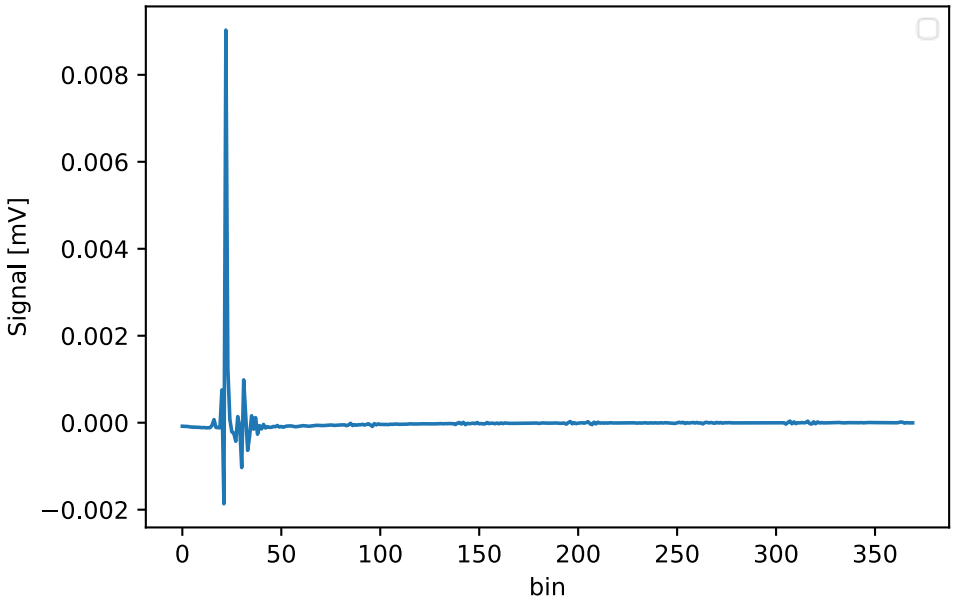

Figure 15: Example of dark measurement of the system MARCO.

4.1.2 Bin Shift

Analog and the photon counting data can have a timing shift between the laser pulse emission and the assumed zero range of the acquired signal. These shifts may be due to the trigger timing or to the electronic processing of the signal. Moreover, different processing times can contribute to a relative shift between analog and photon counting channels.

In case pre-trigger samples are recorded as in the systems described in this thesis, the true "zero" bin can be identified under low background conditions by the signal coming from straylight reflected from the quartz window and container walls. The signals are then shifted accordingly. The values resulted to be consistent between transient recorders of the same system, with differences observed between analog and photon counting modes of acquisition (see Table 9).

Table 9: Expected, and measured analog and photon counting "zero" bins for the systems CONCERNING and MARCO

	Expected	Analog	Photon counting
CONCERNING	1025	1024	1023
MARCO	24	26	25

4.1.3 Dead-time correction

In a non-paralyzable detection system, an event will not be recorded when the time interval between its occurrence and the occurrence of the last recorded event is smaller than the dead-time τ_{DT}. Increasing the event rate, the detection system (detector, pre-amplifier, counter) will reach a saturation rate equal to the inverse of the dead-time.

If $P(z)$ is the measured photon count rate in a time interval Δt, the corrected photon-counting signal will be [49]:

$$P'(z) = \frac{P(z)}{1 - \frac{\tau_{DT}}{\Delta t} P(z)}$$

From a numerical point of view, this equation could be applied as long as $\frac{\tau_{DT}}{\Delta t} P(z) < 1$, in practice however this correction is only valid up to counting rates of a few tens of MHz for typical dead-times of about 1-10 ns (see Figure 16). For higher count rates, the gluing procedure is needed, as the analog signal is not affected by the dead-time effect. A value of 4 ns was found to correct the signal up to 20-30 MHz and was used for all the photon counting channels.

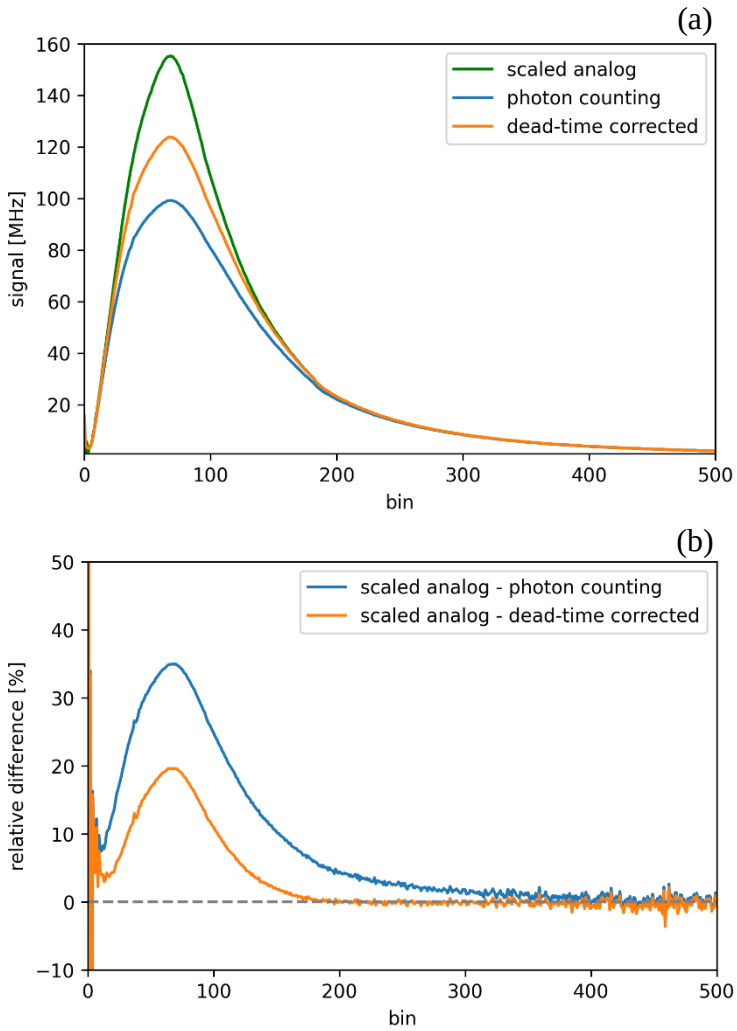

Figure 16: (a) scaled analog, photon counting and dead-time corrected photon counting signals (b) relative difference between scaled analog and photon counting signals.

4.1.4 Gluing

The signal-to-noise ratio achievable with photocounting is generally higher than that of the analog signal. On the other hand, the latter is not limited by dead-time. Gluing analog and photon counting signals allows to exploit the high linearity of analog detection for strong signals and the high sensitivity of photon counting detection at low count rates. There is a region where both signals are valid and have a high signal to noise ratio. For the used PMTs, this region extends approximately from 0.5 to 10 MHz (the thresholds used for the next steps) in the photon counting.

After applying the dead-time correction, linear regression coefficients can be calculated in this region, analog data is scaled into photon counting data, and used above 10 MHz (see Figure 17).

If the peak of the corrected photon counting signal is below 10 MHz, gluing is not needed. On the other hand, if the photon counting background signal level (calculated as the mean value in the far range) is higher than the minimum value of 5 MHz only the

scaled analog signal is used, using pre-calculated coefficients with the assumption of a fixed PMT gain.

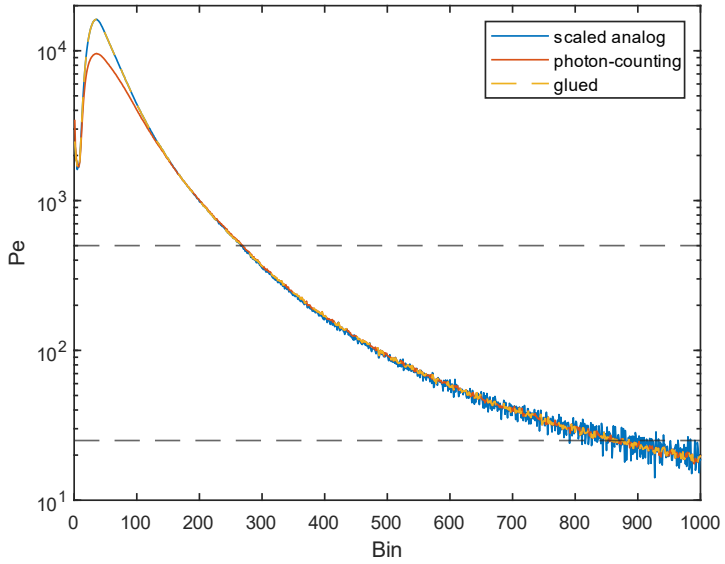

Figure 17: Scaled analog, dead-time corrected photon-counting and glued signals expressed as photoelectrons (Pe). The horizontal lines are the 10 and 0.5 MHz thresholds converted to Pe. The glued signal follows the photon-counting signal under the 10 MHz threshold and the analog signal over the 10 MHz threshold.

4.1.5 Background subtraction

Background subtraction is then applied to remove the solar background contribution from the signals. The background is estimated by averaging the last bins of the lidar echo, corresponding to very high altitudes, or the pre-trigger bins preceding the laser pulse, if the option is active, for which lidar backscatter echoes are supposed to be negligible and only background radiation contributes to the measured signal.

This assumption holds for the CONCERNING lidar system, having no problem to sample a large time interval. For the system MARCO instead, the high repetition rate only permits a maximum sampling distance of 7.5 km (with the pre-trigger option active), after that a second pulse is produced and another lidar echo begins. At this distance some signal can still be present, leading to errors in the background estimation. The elastic channels are the ones more affected by this problem as the signal at 7.5 km is around 1/3 of the one at 5 km. Moreover, clouds and aerosol are still present at these heights, well inside the troposphere. Apart from upgrading the system with a laser source with a lower repetition rate (for example, 10-5 kHz corresponding to a limiting height of 15-30 km), further development is needed to correctly analyse the already acquired data. A possible envisioned solution is the extrapolation of the lidar signal profile in order to estimate the real background in the absence of clouds and the subtraction of the background “as is” when the signal is fully extinguished within the cloud.

4.1.6 Elastic decontamination

In case of very low signals with respect to the elastic backscattering signal (for instance CO_2 Raman signals) or extreme spectral vicinity of the interference filter bandpass to the emission wavelength (LoJ rotational Raman), the optical filter blocking is not sufficient to avoid unwanted crosstalk from the more intense signal. That elastic signal crosstalk into the CO_2 or LoJ rotational Raman signals can be completely removed if simultaneous and co-located measurements of the elastic signal are available [50, 51]. The approach considers the following equation:

$$P'(z) = P(z) - kP_{355}(z) \tag{30}$$

where $P(z)$ is the contaminated CO_2 or LoJ rotational Raman lidar signal, $P'(z)$ is the effective lidar signal used for the following retrieval steps, $P_{355}(z)$ is the 354.7 nm elastic lidar signal, and k the crosstalk factor. With Equation (30) the effective Raman signal can be determined from the contaminated Raman signal by simply subtracting the 354.7 nm elastic lidar signal from the latter.

An accurate estimate of the crosstalk factor k is needed to minimise potential systematic errors associated with the crosstalk. The factor k is determined analyzing lidar profiles with a strong elastic return (for example, clouds) and removing the excess signal from the channel of interest. For CO_2 retrievals different values are tested, and the value leading to the same mixing ratio before, inside and after the cloud is chosen. For temperature retrievals the value of k leading to temperature values inside the cloud best fitting the temperature values from a nearby radiosonde is used.

4.2 CO_2 retrieval

The CO_2 mixing ratio is obtained from Raman backscattered signals through the following equation [52]:

$$x_{CO2}(z) = F_{cal} \frac{T_{N_2}(z)}{T_{CO_2}(z)} \frac{P_{CO_2}(z)}{P_{N_2}(z)} \tag{31}$$

where $P_{CO2}(z)$ is the pre-processed CO_2 roto-vibrational Raman lidar signal at wavelength λ_{CO2}, while $P_{N2}(z)$ is a temperature-independent reference signal, in this case the pre-processed N_2 ro-vibrational Raman signal, F_{cal} is a calibration constant, $T_{CO2}(z)$ and $T_{N2}(z)$ are the atmospheric transmission terms, which accounts for the different atmospheric transmission by molecules and aerosols at λ_{CO2} and λ_{N2}, respectively.

Other signals, such a temperature-independent combination of the LoJ an HiJ rotational Raman signals, can be used as reference. The N_2 ro-vibrational signal was chosen due to several factors. Firstly, the uncertainty (see Eq. 32) in the retrieved mixing ratios,

wether calculated using the N_2 or LoJ+HiJ reference signals, shows negligible differences. This is due to the fact that these uncertainties are primarily driven by the low CO_2 signal-to-noise ratio. Additionally, using the N_2 signal requires less atmospheric transmission correction. Finally, the N_2 channel is the most similar to the CO_2 one in terms of optical path inside the lidar receiver, offering advantages in relative signal stability.

The calibration constant F_{cal} can be determined with in-situ measurements or, as in this work, using the day-time lidar background signal (Section 6.1).

Assuming Poissonian statistics for the signals (that is, assuming that the major source of uncertainty is due to shot noise), the uncertainty affecting CO_2 mixing ratio measurements can be calculated through error propagation as:

$$\Delta x_{CO2} = \frac{x_{CO2}}{\sqrt{mn}} \sqrt{\frac{P_{CO_2}+B_{CO_2}}{P_{CO_2}^2} + \frac{P_{N_2}+B_{N_2}}{P_{N_2}^2}} \tag{32}$$

where B_{CO_2} and B_{N_2} are the measured background signals in the CO_2 and N_2 channels, respectively, m is the number of profiles, and n is the number of vertical bins used for the signal averaging.

4.3 Other algorithms: WV, Temperature, Backscatter

The water vapor mixing ratio (WVMR) is obtained from the ratio of the ro-vibrational H_2O signal to a temperature-independent reference signal [52]:

$$WVMR\,(z) = F_{cal}\,\frac{T_{N_2}(z)}{T_{WV}(z)}\frac{P_{WV}(z)}{P_{N_2}(z)} \tag{33}$$

Here again the reference signal can be the ro-vibrational N_2 signal or a weighted sum of HiJ and LoJ rotational signals. The calibration constant is usually determined by a comparison with co-located measurements, for example radiosondes, or model data.

The statistical uncertainty affecting WVMR measurements can be calculated as:

$$\Delta WVMR = \frac{WVMR}{\sqrt{mn}} \sqrt{\frac{P_{WV}+B_{WV}}{P_{WV}^2} + \frac{P_{N_2}+B_{N_2}}{P_{N_2}^2}} \tag{34}$$

where B_{WV} is the measured background signal in the WV channel.

Exploiting the temperature dependence of the rotational Raman signals, atmospheric temperature profiles can be obtained from the ratio $R(z) = P_{LoJ}(z)/P_{HiJ}(z)$ between

LoJ and HiJ lidar signals. Using a two-parameter relation [11], temperature can be calculated as:

$$T(z) = \frac{b}{ln\, R(z) - a} \tag{35}$$

As with WVMR, the calibration parameters a and b are determined via comparison with co-located radiosondes or reanalysis data. The statistical uncertainty affecting temperature measurements can be again determined through error propagation:

$$\Delta T = \frac{T}{\sqrt{mn}} \frac{dT}{dR} \sqrt{\frac{P_{LoJ} + B_{LoJ}}{P_{LoJ}^2} + \frac{P_{HiJ} + B_{HiJ}}{P_{HiJ}^2}} \tag{36}$$

Finally, the aerosol backscattering coefficients can be retrieved via a variety of techniques, for example using only the elastic signal as in the Klett-Fernald method [53, 54] or in the iterative method [55]. Another possible method takes advantage of the Raman technique, and unlike the previous ones, it does not rely on assumptions on the lidar ratio, that is, on the aerosol type, and does not need corrections in the lower portion of the profile, where partial overlap between the beam and the telescope FOV affects the measurements. Aerosol backscatter coefficient at 355 nm is calculated as [16]:

$$\beta_{aer}(z) = \mathrm{k} \frac{T_{N2}(z)}{T_{355}(z)} \frac{P_{355}(z)}{P_{N_2}(z)} \rho(z) - \beta_{mol}(z) \tag{37}$$

where $P_{355}(z)$ is the total elastic pre-processed signal and $T_{355}(z)$ is the atmospheric transmission at 354.7 nm, $\rho(z)$ is the atmospheric density and k is a calibration constant calculated at a reference height z_0 with negligible aerosol load:

$$\mathrm{k} = \frac{\mathrm{T}_{355}(\mathrm{z}_0)}{\mathrm{T}_{\mathrm{N2}}(\mathrm{z}_0)} \frac{\mathrm{P}_{\mathrm{N2}}(\mathrm{z}_0)}{\mathrm{P}_{355}(\mathrm{z}_0)} \frac{\beta_{\mathrm{mol}}(\mathrm{z}_0)}{\rho(\mathrm{z}_0)} \tag{38}$$

5 Measurement campaigns

5.1 WaLiNeAs

After a short test period in Potenza, the systems CONCERNING and MARCO were deployed in Southern France in the frame of the WaLiNeAs (Water Vapor Lidar Network Assimilation) experiment. This field campaign served as an initial testing ground for the two instruments.

WaLiNeAs, primarily funded by the French National Research Agency (ANR), is an international field experiment aimed at filling an observational gap in the low troposphere, studying extreme precipitation events and enhance their predictability through the assimilation of water vapor profile measurements from a network of Raman lidar systems into mesoscale numerical weather prediction (NWP) models. The implementation of an integrated prediction tool, coupling network measurements of WV profiles and a NWP model would help to estimate the amount, timing and locations of rainfall associated with these events up to 48 h in advance [56], which would be extremely beneficial for the reduction of social and economic impacts, and threats to human lives. The experiment has a specific geographical focus on Southern France, where these events have a high probability of occurring. The measurement strategy implied the exploitation of eight Raman lidars (with the participation of French, German, Spanish and Italian research groups) deployed along the Mediterranean coasts of Spain and France, capable to provide real-time measurements of water vapor mixing ratio profiles over a three-month period starting on October 2022.

Figure 18: Deployment sites of CONCERNING and MARCO in the southern France.

Figure 19: (a) System CONCERNING and CNR-IMAA wind lidar deployed at the University of Toulon, La Garde (Lat.: 43.136040 N, Lon.: 6.011650 E, Elev.: 65 m a.s.l.); (b) system MARCO deployed at the Direction de Services Techniques, Port-Saint-Louis-du-Rhône (Lat.: 43.392570 N, Lon.: 4.813480 E, Elev.: 5 m a.s.l.).

The system CONCERNING was deployed at the University of Toulon, La Garde (Lat.: 43.136040 N, Lon.: 6.011650 E, Elev.: 65 m a.s.l.), together with a wind lidar (Halo Photonics, model: Stream Line XR) made available from CNR-IMAA (Figure 19) and started operation on 29 September 2022, performing 118 days of continuous measurements till 25 January 2023, when a laser failure forced the stop of the operations. Subsequent inspections highlighted internal corrosion problems within the laser head (due to a manufacturing defect) which was promptly sent for maintenance. The system MARCO, was deployed at the Direction de Services Techniques, Port-Saint-Louis-du-Rhône (Lat.: 43.392570 N, Lon.: 4.813480 E, Elev.: 5 m a.s.l.), with continuous measurements since 19 October 2022. MARCO was operated for an extended period of 16 months till 22 February 2024, successfully demonstrating the capability of a Raman lidar based on a micro-pulse laser source.

The acquired profiles had to be assimilated in near real-time, with updates every 15-30 minutes, in the AROME-France model (Application of Research to Operations at MEsoscale). For the WaLiNeAs campaign, the system CONCERNING was operated with a raw vertical resolution of 7.5 m and temporal resolution of 10 s up to 40 km, while MARCO, due to limitations of the acquisition hardware coupled with its high repetition rate, had a vertical resolution of 15 m and temporal resolution of 3 s up to 5 km. Data was uploaded to a Network Attached Storage (NAS) and analysed every 15 minutes for CONCERNING and every 30 minutes for MARCO in order to provide near real-time measurements of water vapor mixing ratio. The coarser time resolution of the latter was chosen for achieving a better signal-to-noise ratio. For each system data was down-sampled to a vertical resolution of 100 m in order to improve the signal-to-noise ratio, especially required for daytime measurements. The profiles were then uploaded on the Météo-France server in a specified format, ready for the assimilation in the AROME-France model. This exercise successfully demonstrated the operational readiness of a network of such instruments.

The first release of the dataset was produced using only analog data and skipping the gluing step, still not ready at the start of the campaign and requiring manual inspection of the results. The calibration constant was calculated taking advance of co-located radiosondes in Potenza and confirmed to be stable during the campaign (see Figure 20).

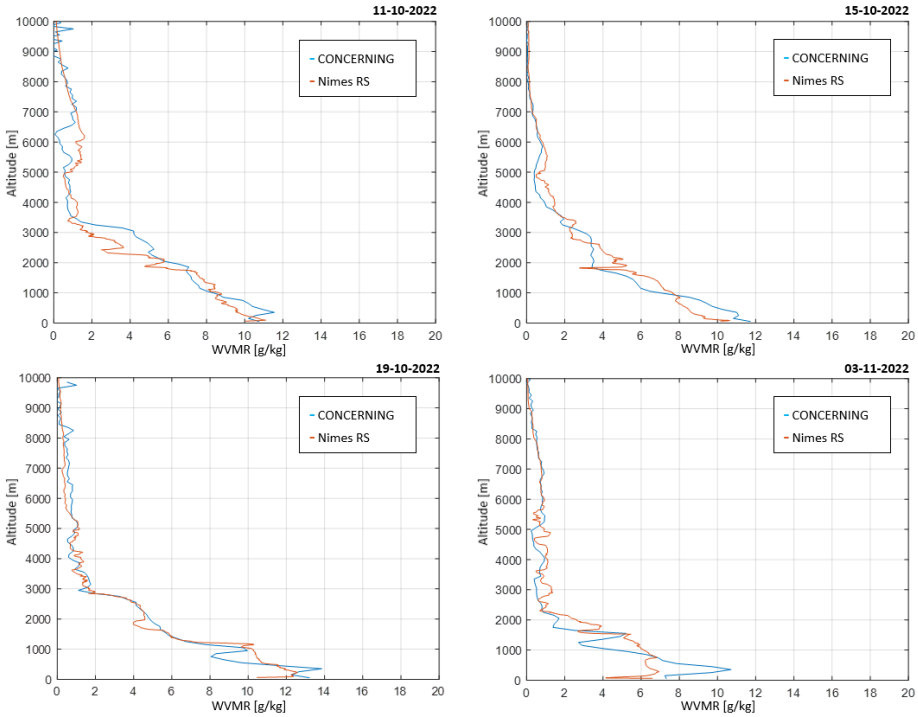

Figure 20: Comparison between CONCERNING WVMR profiles and 00:00 UTC radiosonde data from the Nimes-Courbessac launch site [57].

Figure 21 shows four consecutive months of water vapor measurements obtained with the system CONCERNING. The system demonstrated excellent performance during both night-time and daytime and recorded several heavy precipitation events (>100 mm of cumulated rain during 24 h), including three weather watch alerts in neighbouring French departments, on 20-21 October, 31 October, 8-9 November and 14 November 2022. Especially the second half of October shows high concentrations of water vapor, with an expected decrease moving towards the winter months. This trend is evident in the monthly averages shown in Figure 22, which also illustrate the gradual daytime increase in the mixing ratio and the daily evolution of the boundary layer, with its height decreasing going towards the winter months. Figures 23 and 24 show 16 months of measurements performed by the system MARCO. The figures clearly reveal the seasonal variation of water vapor concentration, with values ranging from 10-15 g/kg during summer to 5-10 g/kg in winter. High solar background signal prevented accurate measurements during daytime in summer months. The system shows good performance during night-time, even if the system performance suffers a natural decline over the months due to laser power losses. Dirt from wind and precipitation, and the accumulation of insects, strongly attracted by the UV light, heavily affected the instrument performance and the capability to correctly align the system, especially during summer months. This problem was mitigated with periodic on-site inspections and maintenance, and the performance of the system at the end of the campaign was only slightly degraded despite the long period of operation.

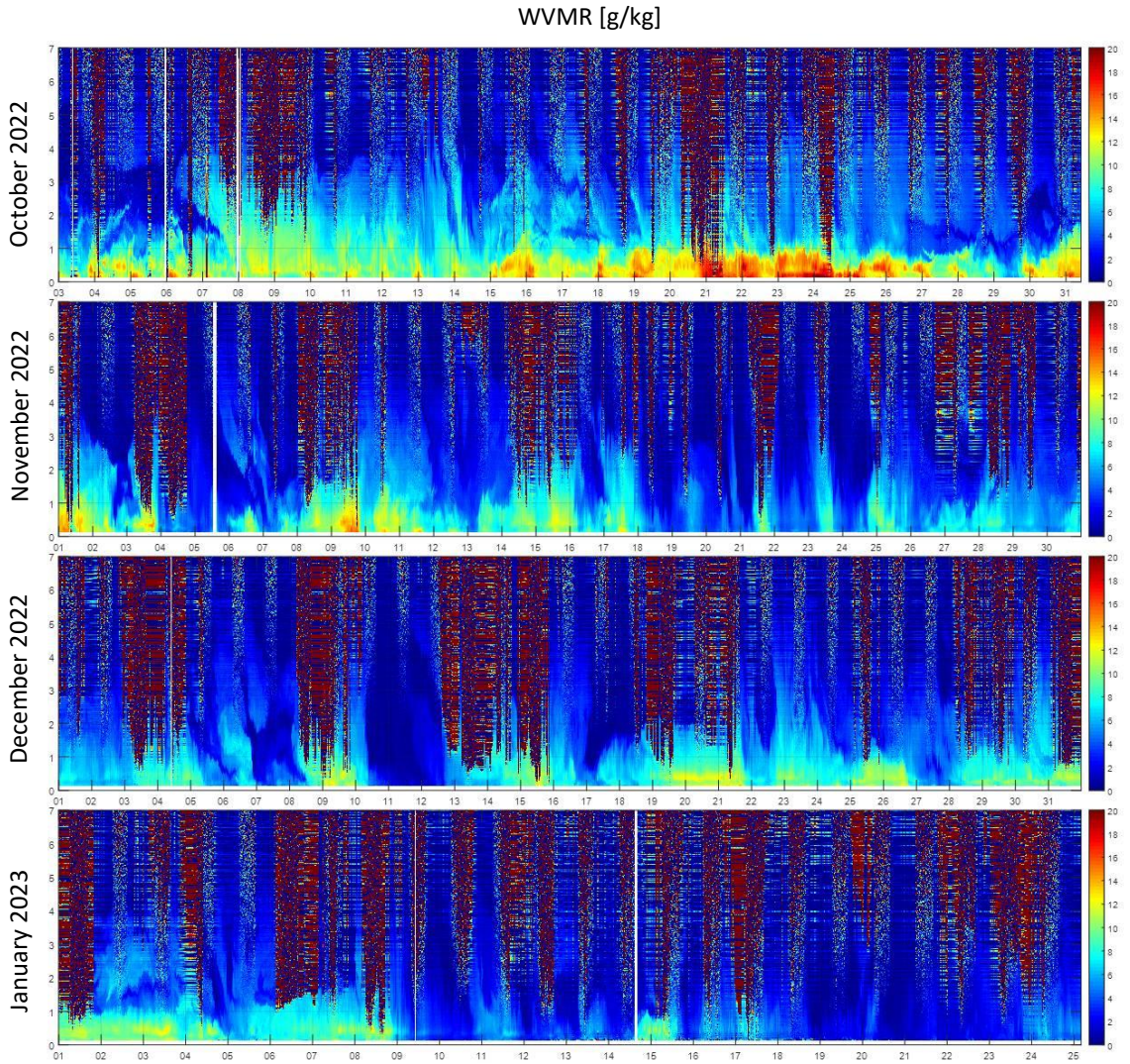

Figure 21: WVMR measurements made by CONCERNING during WaLiNeAs campaign at full vertical resolution (7.5 m) and 15 min temporal resolution.

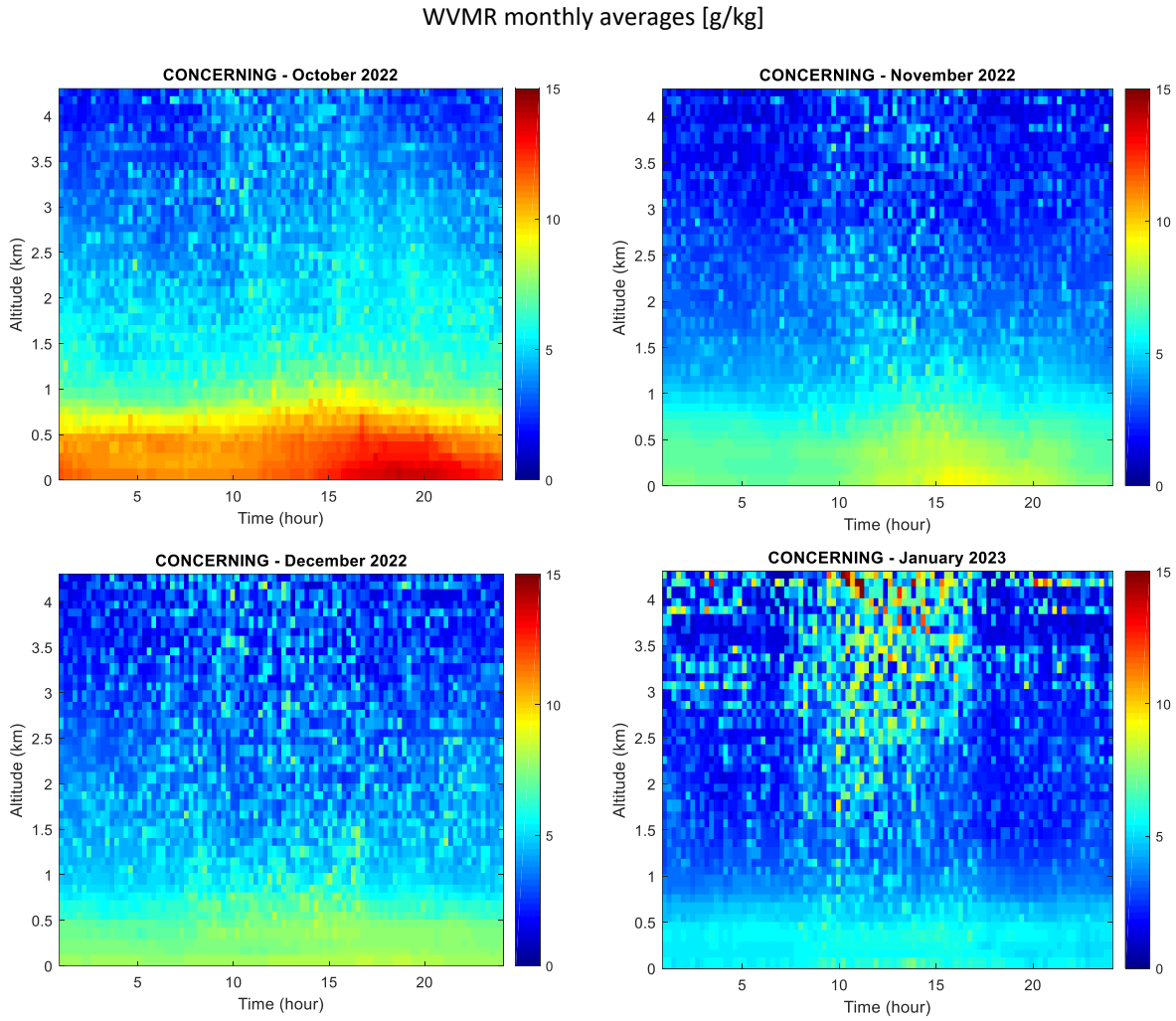

Figure 22: Monthly WVMR as measured by system CONCERNING.

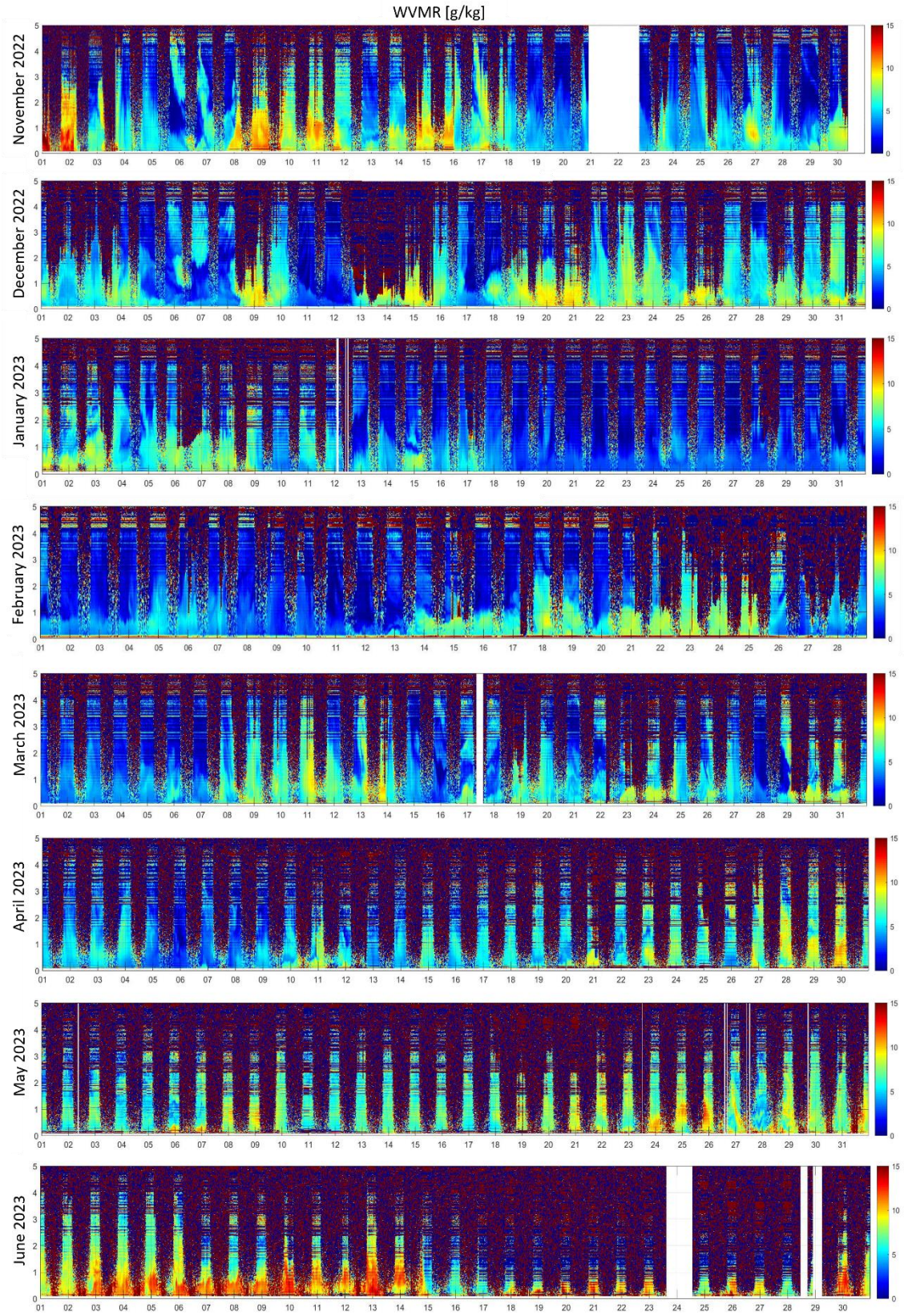

Figure 23: WVMR measurements (November 2022 – June 2023) made by MARCO during WaLiNeAs campaign at 30 m vertical resolution and 30 min temporal resolution.

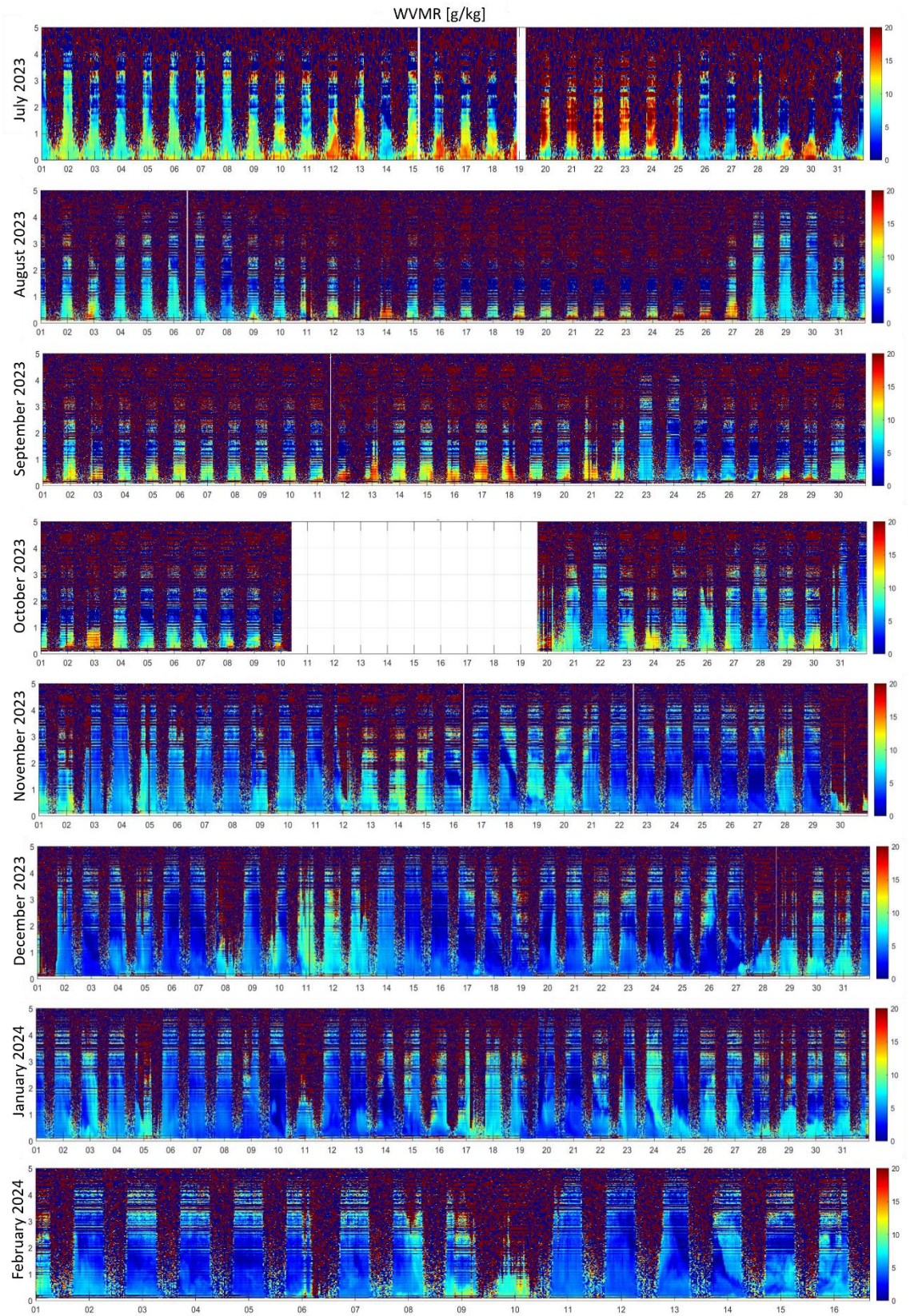

Figure 24: WVMR measurements (July 2023 – February 2024) made by MARCO during WaLiNeAs campaign at 30 m vertical resolution and 30 min temporal resolution.

Data collected by the two systems will be part of deeper studies in future research activities. These include the study of turbulent processes with the measurement of latent heat flows using simultaneous high temporal resolution data of water vapor mixing ratio from CONCERNING and vertical wind components from the co-located wind lidar. Latent heat release enhances convective processes, contributing to the vertical movement of air, cloud development, and the redistribution of heat within the atmosphere. Three cloud-free 30-minute analysis periods followed by precipitation events were selected as case-studies (31 October, 28 November, and 8 December 2022). Figure 25 shows latent heat flux profiles for the selected case-studies calculated with the eddy covariance method [58, 59]. The results show typical latent heat flux profiles, with positive values in the boundary layer, representing a significant upward humidity transport. The values are correlated with the turbulent kinetic energy profiles calculated from wind lidar data and with the intensity of the following precipitation events.

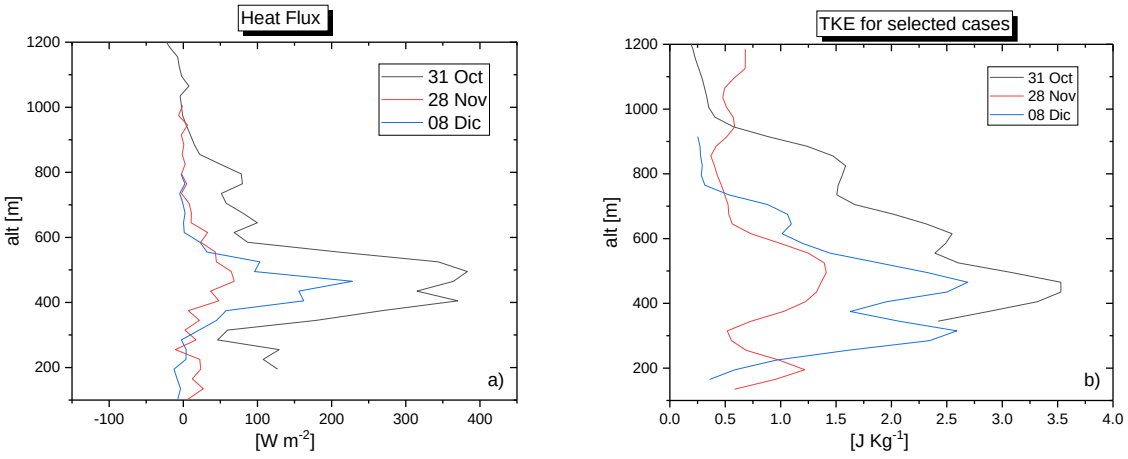

Figure 25: (a) Latent heat flux profiles calculated using WVMR data in combination with wind lidar data for selected cases during the WaLiNeAs campaign (b) Turbulent kinetic energy calculated from wind lidar data.

Selected cases (for example, 13-17 November 2022, see Figure 26) coincident to heavy precipitation events are also being analized separately for the assimilation into the Weather Research and Forecasting (WRF) model [60]. Data for these cases have been processed applying all the pre-processing steps, gluing included, with the addition of quality checks such as uncertainty thresholds ($\sigma_{WVMR} \leq 1$ g/kg) and value thresholds ($0 \leq$ WVMR ≤ 25 g/kg) on the retrieved mixing ratio.

Using both analog and photon-counting data greatly improves the measurement quality in both systems. The complete workflow, tested for a restricted number of cases, is now being extended to the rest of the dataset for the production of a second refined release.

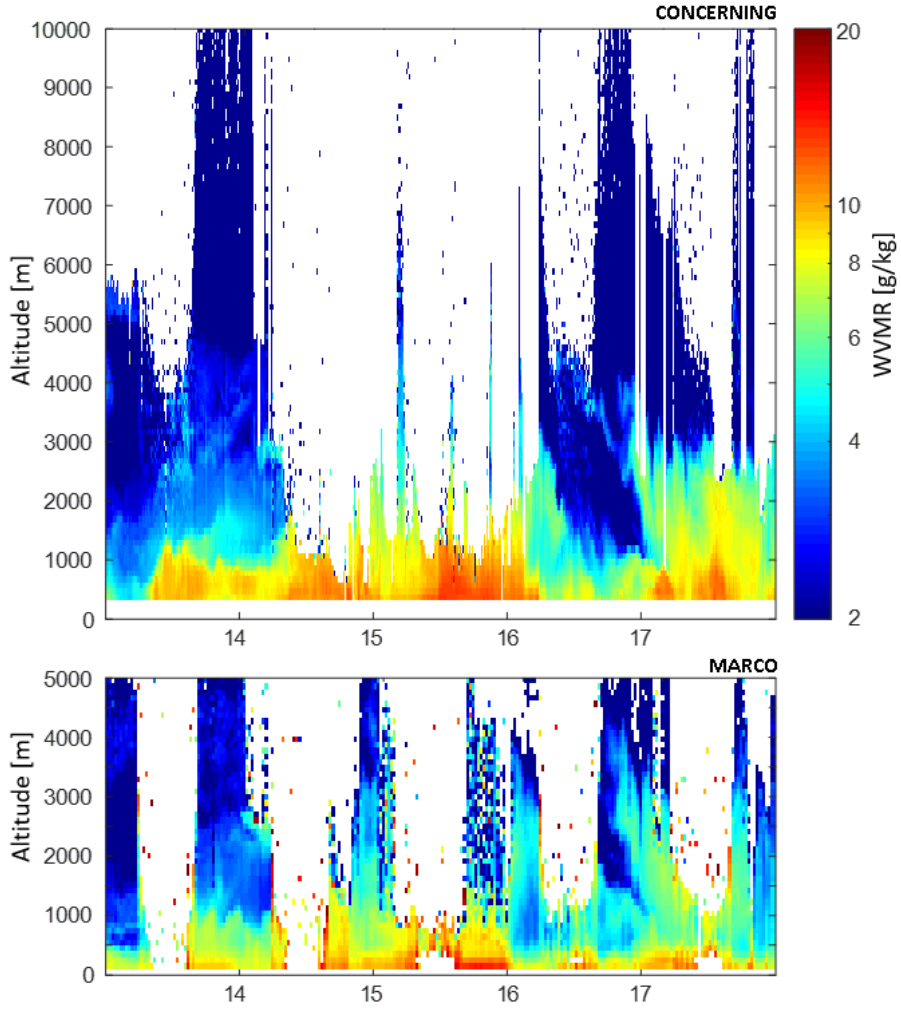

Figure 26: Reprocessed and quality-controlled WVMR measurements (13-17 November 2022) at 100 m vertical resolution, and 15 min and 30 min temporal resolution for CONCERNING and MARCO, respectively.

5.2 BELLA

The BELLA (Boundary layer Extensive campaign with muLti instrumentaL Analisys) / ABL-ITINERIS measurement campaign took place in Potenza, Italy between April and May 2024 [61]. This campaign has been organized by CNR-IMAA in collaboration with UNIBAS with the main goal to establish a comprehensive dataset for the study of the Atmospheric Boundary Layer (ABL) height evolution and for the characterization of physical and chemical processes taking place within both the ABL and the troposphere. The system CONCERNING (Lat: 40.647477 N, Lon: 15.807204 E, Elev: 710 m a.s.l.) was continuously active during the campaign period, taking measurements in coordination with CIAO observatory instruments [62]. All the sensors have been operating continuously during the campaign under different atmospheric conditions. The resulting dataset, acquired between 14 April 2024 and 06 May 2024, is of interest for several purposes like the testing and the assessment of new ABL height retrieval algorithms, a better understanding of the processes occurring in the lower atmosphere taking advantage of a multi-sensor approach, and the validation of mesoscale atmospheric models. Figure 27 shows some of the products of the campaign, in particular the retrieved vertical timeseries of aerosol backscattering coefficient, the water vapor mixing ratio, and the atmospheric temperature. The two measurement gaps in the third week are due to the laser head overheating, causing a system halt. Water leaks from the laser head were detected after the second stop and further inspection reconducted this anomaly to the same problem encountered during the WaLiNeAs campaign, the laser was therefore sent again for maintenance. The produced dataset is currently being analysed.

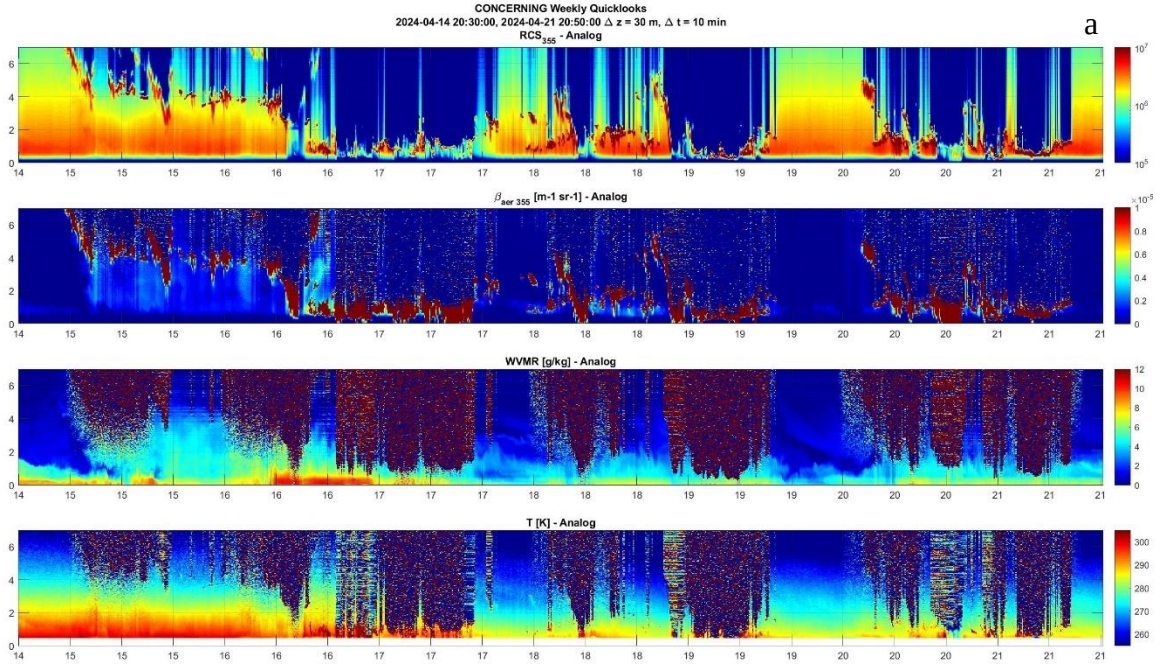

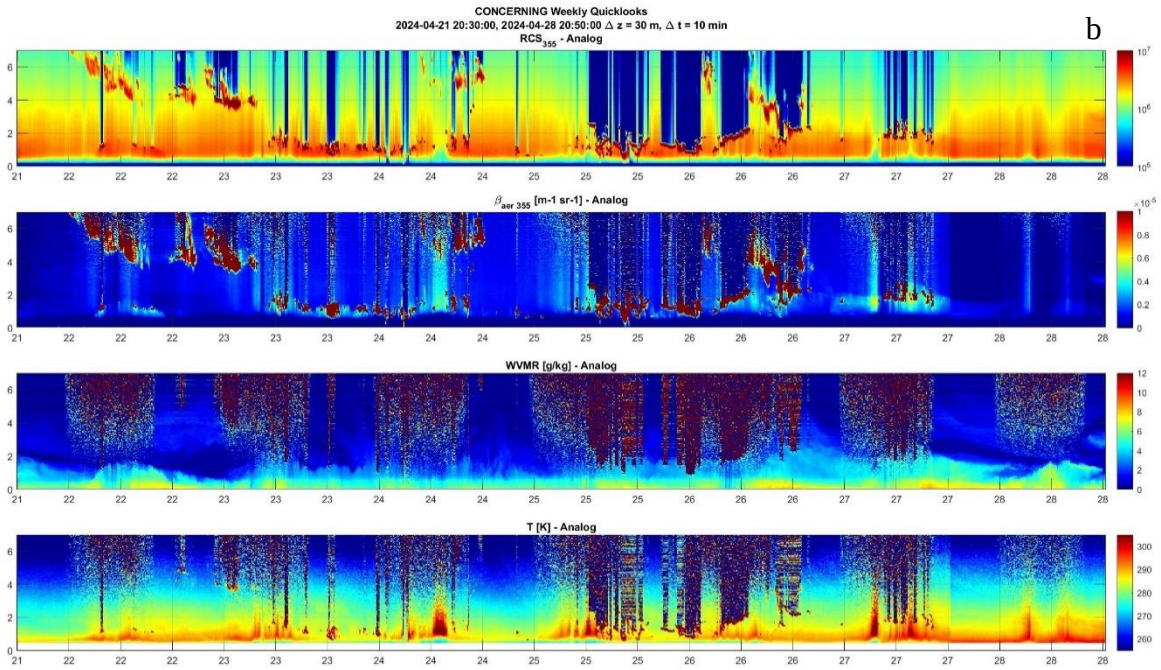

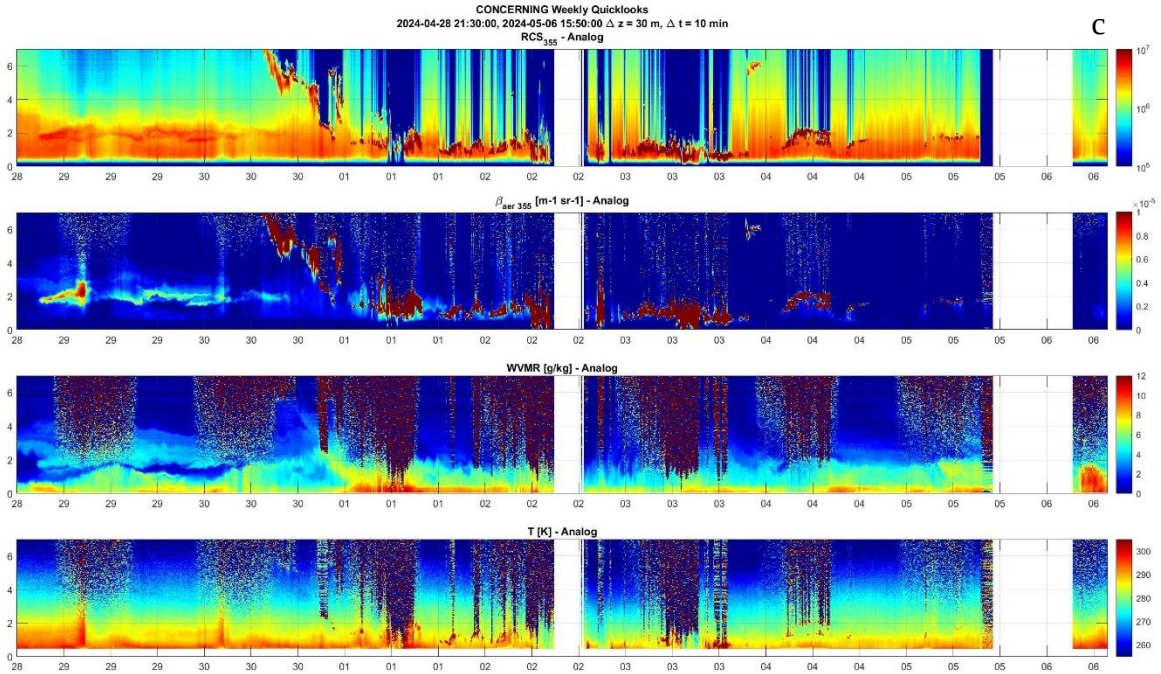

Figure 27: (a, b, c) Weekly quicklooks of BELLA campaign products from 14 April 2024 to 06 May 2024: range-corrected signal (RCS) at 355 nm, aerosol backscattering coefficient, WV mixing ratio, and temperature.

5.3 DECIPHER

DECIPHER (Disentangling mechanisms controlling atmospheric transport and mixing processes over mountain areas at different space- and timescales) is the last field campaign in which the system MARCO was involved. The project, funded by the Italian Ministry of University and Research and organized by the University of Trento, is part of the international TEAMx (multi-scale Transport and Exchange processes in the Atmosphere over Mountains – programme and eXperiment) program [63].

The project aims at improving the understanding of processes controlling exchange of momentum, energy and substances between the Earth surface and the atmosphere over mountains, transport processes across a variety of scales, including turbulent mixing and removal by precipitation scavenging, and evaluating how well these are represented in NWP and climate models. Field measurements have and will be performed with multiple instruments during 2024 and 2025 at two selected target areas representative of two different mountain situations: the isolated peak of Col Margherita (Eastern Italian Alps) and an extended slope on a side of Monte Baldo (Central Italian Alps).

A first part of the measurement campaign started on 27 July 2024, when the system MARCO was deployed (Figure 28) at Passo Valles, Trento, Italy (Lat: 46,338469 N, Lon: 11.799588 E, Elev: 2032 m a.s.l.) near Col Margherita CNR-ISP observatory [64] and next to the wind lidar (Leosphere WINDCUBE 100s) of the University of Trento and a weather station managed by Meteo Trentino.

Figure 28: System MARCO next to the wind lidar during the DECIPHER campaign.

The synergic use of the two instruments (for example, applied to measurements of vertical profiles of latent and sensible heat fluxes) will allow to carry out fundamental measurements for a full understanding of meteorological phenomena occurring in the alpine area and of the turbulent properties characteristic of mountain atmosphere.

The system measurements are particularly effective for the purposes of the DECIPHER project. Specifically, they will contribute to understanding the mechanisms that at different spatial and temporal scales control atmospheric transport and mixing processes in mountain areas, characterizing turbulent processes in the ABL on mountain slopes, and, in general, surface-atmosphere exchange processes.

Some extraordinary maintenance operations were necessary before the start of the campaign such as the re-waterproofing of the roof (some leaks had been noticed at the end of the WaLiNeAs campaign) and the replacement of the controller of the 45-degree steering mirror motors. The mirror itself was replaced as the dielectric coating had been partially ablated by the incoming UV radiation. Moreover, specific upgrades to the system have been implemented for the campaign. A 5x beam expander has been added to improve the stability of the lidar signal: reduced beam divergence should improve the stability of the beam overlap with the telescope's field of view. Furthermore, the expanded beam should make the system less sensitive to dirt accumulation at the specific point where the beam passes through the quartz window. Additionally, LoJ and HiJ rotational Raman interference filters have been added, along with two additional PMTs and transient recorders, adding the ability to measure temperature profiles.

It has to be noted that the combination of a reduced laser power (2.5 W) due to the aging of the laser diodes and the addition of the beam expander, allow the system to be eye-safe for short exposures times (<1 s) right from the exit aperture.

Figure 29 shows the quicklooks of range corrected signal at 355nm (RCS), the water vapor mixing ratio (WVMR) and the atmospheric temperature (T) measured by MARCO during the initial weeks of the DECIPHER campaign.

a

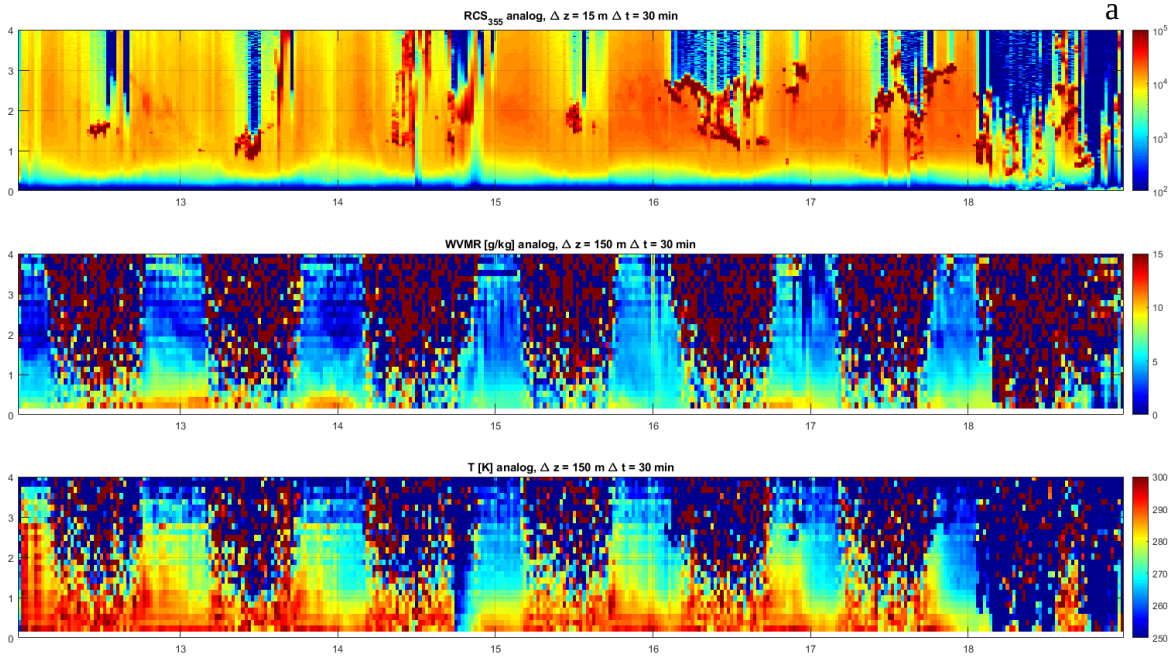
RCS355 analog, Δ z = 15 m Δ t = 30 min
WVMR [g/kg] analog, Δ z = 150 m Δ t = 30 min
T [K] analog, Δ z = 150 m Δ t = 30 min

b

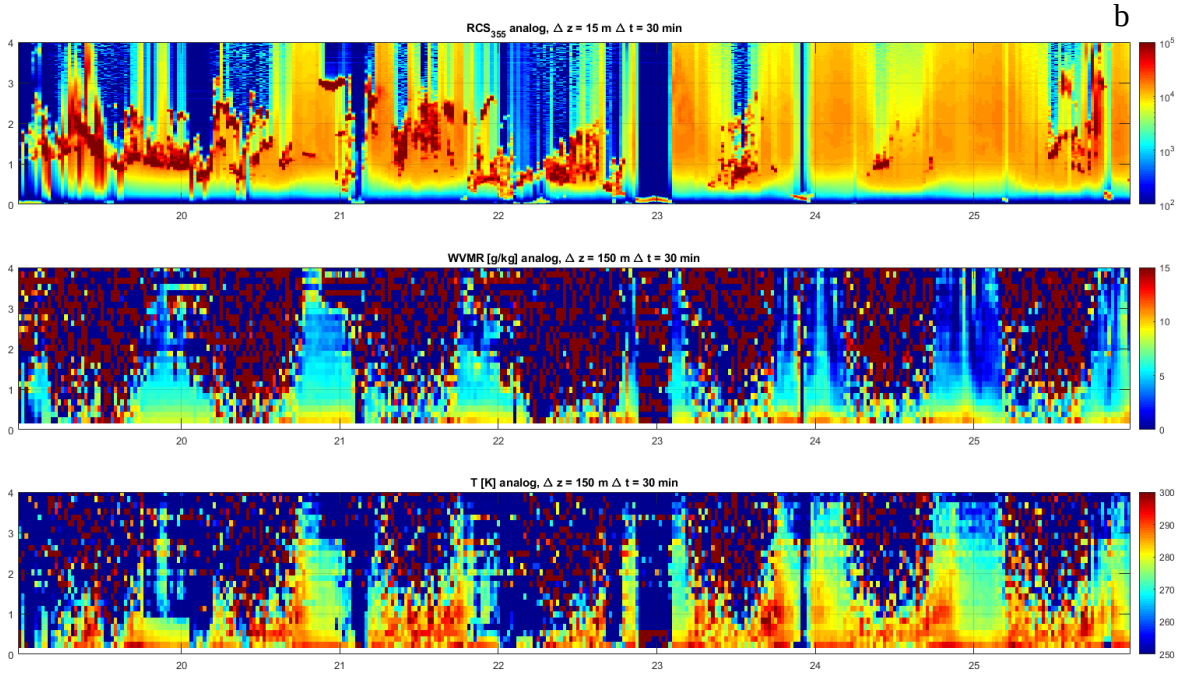
RCS355 analog, Δ z = 15 m Δ t = 30 min
WVMR [g/kg] analog, Δ z = 150 m Δ t = 30 min
T [K] analog, Δ z = 150 m Δ t = 30 min

c

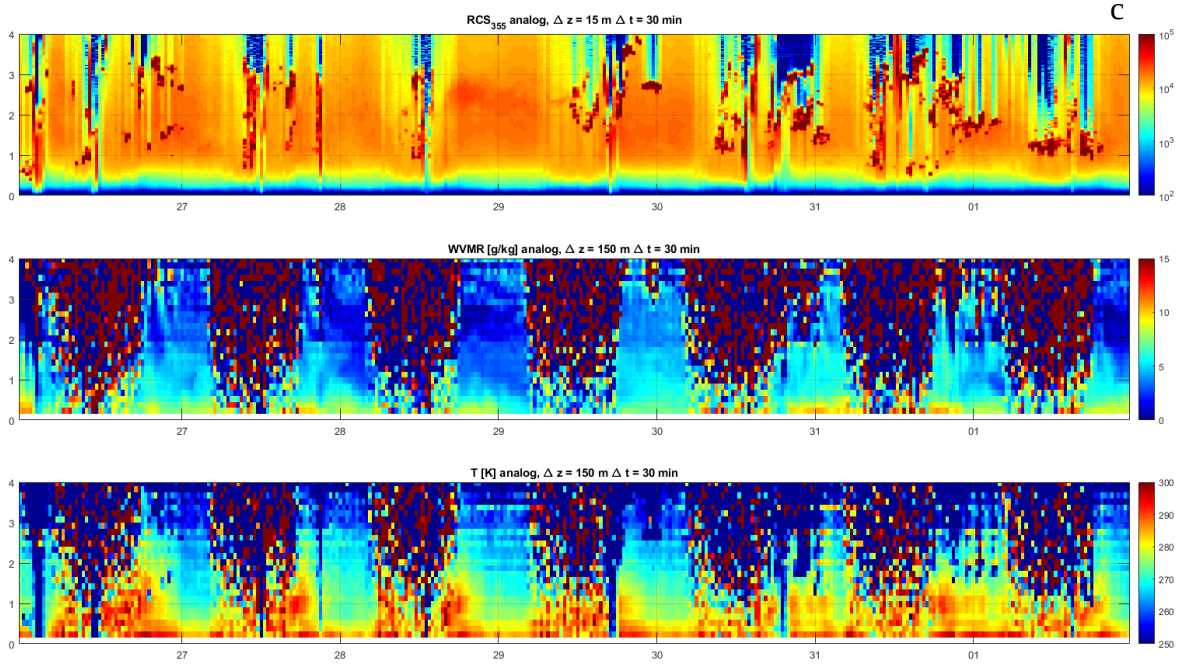

Figure 29: (a, b, c) Weekly quicklooks of DECIPHER campaign products from 12 August 2024 to 01 September 2024: range-corrected signal (RCS) at 355 nm, WV mixing ratio (WVMR), and temperature (T).

6 CO2 Measurements

6.1 Calibration

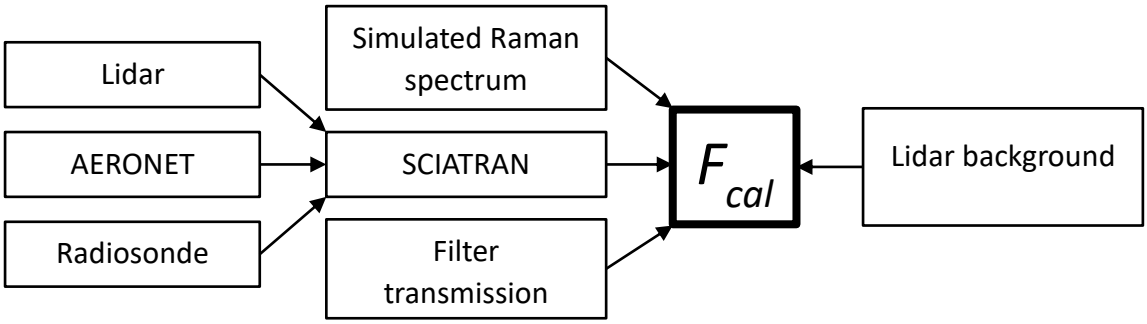

Figure 30: Schematics of the calibration algorithm and inputs.

For CO_2 mixing ratio measurements with the Raman lidar technique, the calibration constant F_{cal} was usually retrieved via comparison with in-situ measurements [12, 18] or could be calibrated using an estimated and fixed mixing ratio at high altitude. Ground-based measurements sample in a blind region for lidar, while air-borne measurements, although ideal for calibration, are more difficult to perform. Lastly, calibrating at higher altitudes, where CO_2 mixing ratio is expected to be constant, would mean to deal with a portion of the lidar signal typically suffering from very low SNR, with resulting mixing ratio accuracies in the order of 10 ppm or more. For these reasons a new technique was adopted and the constant was estimated independently using the day-time lidar background signal, proportional to the zenithal sky radiance. This technique, first described by Sherlock et al. [65, 66] for water vapor Raman lidar measurements, was adapted to CO_2 measurements:

$$\mathrm{F_{cal}} = 0.7808 \frac{\left(\frac{\mathrm{d}\sigma_{\mathrm{N2}}}{d\Omega}\right)_{eff}}{\left(\frac{\mathrm{d}\sigma_{\mathrm{CO2}}}{d\Omega}\right)_{eff}} \frac{K_{N2}}{K_{CO2}} \tag{39}$$

$$\left(\frac{\mathrm{d}\sigma_{\mathrm{X}}}{d\Omega}\right)_{eff} = \sum_i \frac{\mathrm{d}\sigma_{\mathrm{X}}}{d\Omega}(\lambda_i)\ \tau_X(\lambda_i) \tag{40}$$

$$\frac{K_{N2}}{K_{CO2}} = \frac{L_{\lambda_{CO2}}}{L_{\lambda_{N2}}} \frac{B_{N2}}{B_{CO2}} \tag{41}$$

$$L_{\lambda X} = \int L(\lambda)\tau_X(\lambda)d\lambda \tag{42}$$

where $(d\sigma_X/d\Omega)_{eff}$ is the effective cross section (that is, the sum over λ_i of the Raman cross section weighted by the filter transmittance τ_X), $L_{\lambda X}$ is the effective radiance (that is, the spectral radiance L weighted by the filter transmittance), and B_X is the measured background signal. The Raman cross sections (Figure 31) were computed with the simulator code (see Section 1.1.3), and the spectral radiance (Figure 32) was estimated with the SCIATRAN radiative transfer model. As the CO_2 dichroic beam splitter has different transmittances at 386.7 nm for the two polarization components (Ts and Tp, see Figure 32b), the effective radiance was calculated taking into account the polarization of the radiance. Dichroic filters with similar transmittance/reflectivity of the two polarization components were neglected in the calculations. Filter and dichroic measured transmittances were provided by the manufacturers. A scheme of the calibration algorithm and inputs is represented in Figure 30.

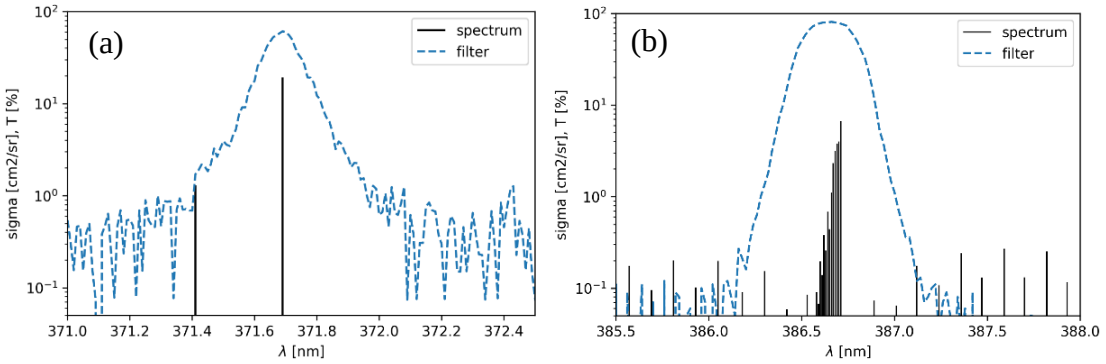

Figure 31: (a) Carbon dioxide vibrational Raman spectrum, calculated at 280 K, and transmittance of the interference filter of the 371.69 nm channel (blue dashed line). (b) Nitrogen ro-vibrational Raman spectrum, calculated at 280 K, and transmittance of the interference filter of the 386.7 nm channel (blue dashed line).

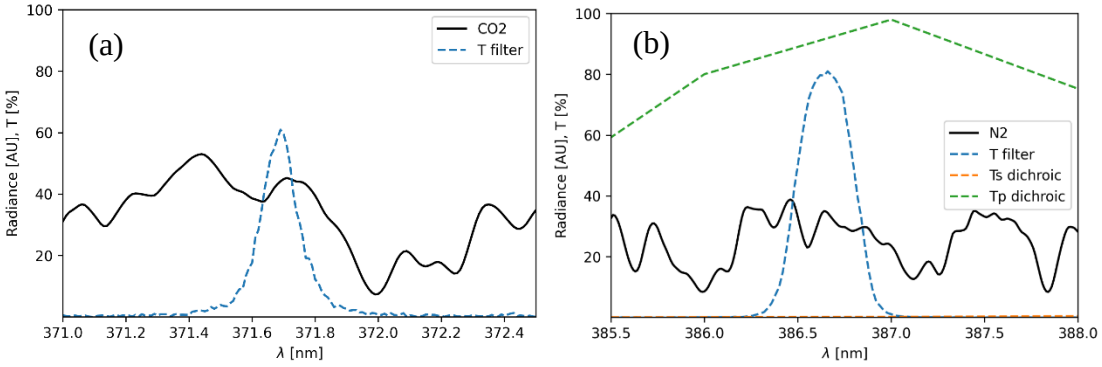

Figure 32: (a) Spectral radiance and transmittance of the interference filter of the 371.7 nm channel (blue dashed line). (b) Spectral radiance and transmittance of the interference filter and the dichroic filters of the 386.7 nm channel (dashed lines).

6.2 **Results**

The CO_2 mixing ratio measurements presented in this section refer to observations made by CONCERNING on 22 January 2024. The system was located at the School of Engineering of the University of Basilicata (40.647477 N, 15.807204 E, 710 m a.s.l.), Potenza, Italy. Being the calibration approach robust with respect to the diurnal cycle of the CO_2 mixing ratio, the day-time portion of the measurement session (13:40-14:00 UTC) was used for the calibration, while night-time (17:00-19:00 UTC) measurements were instead used for the CO_2 mixing ratio profile retrieval.

Data from the nearby AERONET [44] station of Tito Scalo, hosted by CNR-IMAA, was used as input to the software SCIATRAN for the calculation of the zenithal sky radiance. The aerosol load in the atmosphere during the calibration session was relatively low, with an aerosol optical depth of $\tau_{380} = 0.092$. The retrieved calibration constant was quite stable over the whole calibration period, with a mean value of $4.957 \cdot 10^{-2}$ and a standard deviation of $3.9 \cdot 10^{-5}$.

Figure 33 shows the calibrated CO_2 mixing ratio profile from 800 to 6000 m. The vertical resolution is 150 m up to 2400 m, 300 m up to 3600 m, and 450 m in the higher portion of the profile. The measurements were integrated over a 2-hour time window.

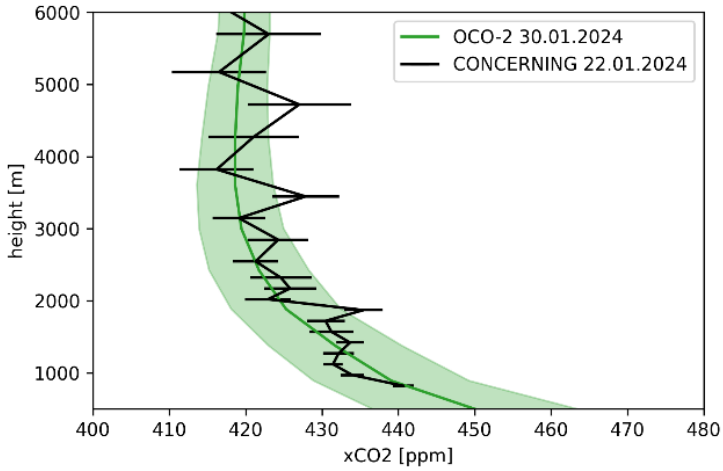

Figure 33: Comparison between lidar (black) and OCO-2 (green) measured CO_2 mixing ratio profiles. The uncertainty of the measurements is represented by horizontal bars and shaded green, respectively.

The obtained profile has an uncertainty Δx_{CO2} < 5 ppm up to 4 km, enough to highlight a clear gradient slightly below 2 km. Measurements under 800 m were discarded, being potentially compromised by overlap issues. In absence of in-situ measurements, a comparison was made with the closest OCO-2 [67] satellite overpass using the closest data point (40.560715 N, 15.84124 E, 30-01-2024 11:51 UTC, see Figure 34). The agreement is within one standard deviation and the lidar profile well captures the fine details in the variability of the lower part of the profile.

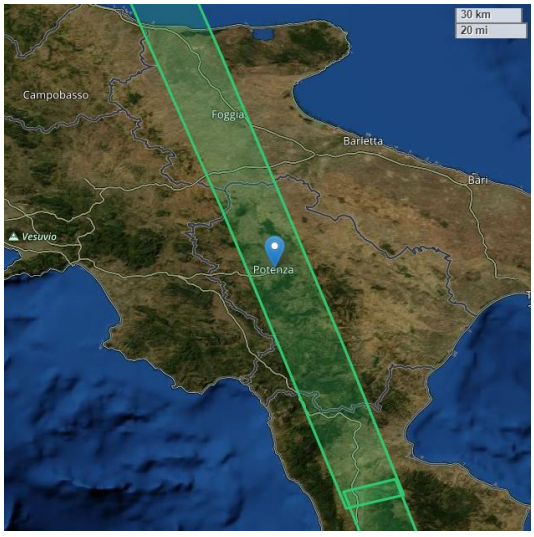

Figure 34: OCO-2 overpass (30 January 2024) footprint and position of the data point used in the comparison (40.560715 N, 15.84124 E).

This case study demonstrates the potential of the instrumental setup and of the adopted technique. Further work will involve consolidating the calibration technique and

estimating a detailed uncertainty budget, in particular addressing uncertainties from aerosols and assumed instrument characteristics. Additionally, significant effort will be directed towards reducing system-derived uncertainties, improving the system's thermo-mechanical stability and eliminating undesired electromagnetic noise that still partially affects the photon counting channels. Comparisons will be made with in-situ CO_2 measurements that will be available from a nearby atmospheric tower, hosted by CNR-IMAA and part of the ICOS network [68], and with coincident OCO-2 overpasses. Lastly, multiple measurement sessions will be analysed in order to evaluate the stability of the calibration constant and to study the time evolution of the mixing ratio profile over extended time periods. The CO_2 measurement capability was available during the BELLA campaign, and the data acquired during this extended period is currently being analysed. A preliminary assessment of the stability of the calibration constant using the aforementioned data was conducted (see Table 10).

Table 10: Preliminary values of the calibration constant during the BELLA campaign

	F_{cal}	σ_{Fcal}
22 January 2024	$4.957 \cdot 10^{-2}$	$3.9 \cdot 10^{-5}$
20 April 2024	$4.113 \cdot 10^{-2}$	$2.5 \cdot 10^{-4}$
28 April 2024	$3.881 \cdot 10^{-2}$	$1.2 \cdot 10^{-3}$
05 May 2024	$3.936 \cdot 10^{-2}$	$1.4 \cdot 10^{-4}$

The retrieved values, calculated over 3-hour periods after sunrise, show significant differences between the sessions and low standard deviations within the sessions, indicating a relatively good short-term stability. The large difference between the January value and subsequent values is attributed to the replacement of the collimation lens, a comprehensive realignment of the system, and adjustments to the photon counting thresholds. The smaller but still significant variation in the calibration constant values during the other calibration sessions may be due to the use of the 22 January aerosol scenario in the preliminary calculations or system alignment instabilities between different sessions and need further investigation.

7 Activities in support of the CALIGOLA mission

The Cloud and Aerosol Lidar for Global Scale Observations of the Ocean-Land-Atmosphere System (CALIGOLA) [14, 69] is an advanced, multi-purpose space lidar mission designed to observe the atmosphere and ocean and to characterize the interactions within the Ocean-Earth-Atmosphere system. Conceived by the Italian Space Agency (ASI), this mission aims to provide the international atmospheric and ocean science communities with an unprecedented dataset of geophysical parameters. This will enhance scientific knowledge in atmospheric, terrestrial, cryospheric, and oceanographic sciences [70]. ASI is collaborating with NASA on this innovative mission, which is scheduled for launch between 2031 and 2032, with an expected operational lifetime of 3-5 years, covering a period not currently addressed by other space lidar missions.

Studies to assess the technological feasibility of the lidar subsystems are currently underway at Leonardo S.p.A. Moreover, NASA Langley Research Center is specifically working on the detectors and the acquisition subsystems. Scientific studies in support of the mission are conducted by the University of Basilicata, with the support of NASA, CNR-ISMAR and CNR-IMAA.

The space-borne Raman lidar CALIGOLA will exploit all the three wavelengths emitted by a Nd:YAG laser source in the UV (354.7 nm), VIS (532 nm) and NIR (1064 nm). It will measure vertical profiles of the particle backscatter coefficient (β_{355}, β_{532}, β_{1064}) at 354.7, 532 and 1064 nm, the depolarization ratio (δ_{355}, δ_{532}) in UV and visible, and the particle extinction coefficient at 354.7 (α_{355}) from aerosols and clouds. CALIGOLA will take advantage, for the first time for a space-borne instrument, of the Raman lidar technique. In particular, in addition to the elastic channels, a temperature independent rotational Raman channel will be used as a reference signal in the atmosphere.

Additionally, measurements of elastic and depolarized backscattered echoes from the sea surface and underlying layers will be conducted to analyse the marine surface and the optical properties of suspended particulate matter. These measurements will be expressed in terms of the oceanic particulate backscattering coefficient (b_{bp}) and the diffuse attenuation coefficient for down-welling irradiance (K_d) at 354.7 nm and potentially 532 nm. The collection of water ro-vibrational Raman signals around 405 nm (β_{H20}), as well as fluorescent scattering measurements at 685 nm (β_{FL685}) will address both atmospheric and oceanic objectives These measurements will enhance our understanding of the role of phytoplankton in marine biogeochemistry, the global carbon cycle, and ocean primary production.

CALIGOLA will finally also assess the small-scale variations in Earth's surface elevation, linked to changes in ice and snow depth, terrain, vegetation, and forest canopy height.

In the framework of the feasibility studies of the lidar subsystems and in line with the activities planned for my industrial doctorate, I completed a six-month internship at Leonardo S.p.A. from November 2022 to May 2023. The activities during the internship period focused on preliminary ray-tracing simulations of transmission and reception optics of the CALIGOLA lidar. Among others, the surface processing requirements of the primary mirror, the transmission efficiency of the telescope, and the effects on the polarization of optics such as the off-axis collimator and the beam expander were estimated.

Regarding the two lidar systems discussed in this thesis, the know-how acquired during the development and testing of the systems CONCERNING and MARCO has proven invaluable for the CALIGOLA mission. The lidar simulator, mutuating the lessons learnt as part of the design and development phases of the systems MARCO and CONCERNING, is currently being integrated with another simulator originally developed at the University of Basilicata in the frame of a previous PhD research program [71], and is being adapted to simulate space-borne lidar signals. The ASI-funded CNR-ISMAR PeRfOrmance simulaTor for ocEan Observations (PROTEO) project aims to support the CALIGOLA mission by enhancing and expanding its scientific and application aspects, particularly in assessing its ocean observation capabilities. The core activity of the project is the development of an end-to-end lidar simulator for ocean color measurements, with the goal of evaluating the specifics of the CALIGOLA lidar system and estimating its expected ocean color performance. Within this framework, SCIATRAN has already been successfully used to simulate lidar background signals over the ocean, and the simulator code discussed in the thesis will serve as a basis for the end-to-end simulator, and expanded to simulate oceanic lidar echoes. Moreover, a similar approach to the one used for the CO2 measurements presented in this thesis will be applied for the vicarious calibration of the 405 nm and 685 nm channels.

The two developed systems served also as a testbed for several state-of-the-art solutions and techniques that will be adopted in the CALIGOLA mission. Above all, the use of the Raman lidar technique, that is an absolute novelty for a space-borne lidar. Some of the processing and retrieval algorithms tested with the ground-based lidars will be adapted and implemented for the CALIGOLA lidar mission. Moreover, the combined acquisition of analog and photon-counting data is also envisioned for the first time in a space-borne lidar system. This approach allows for a dynamic range spanning over more than six orders of magnitude in the lidar signal, enabling the acquisition of strong returns from clouds and ocean surface without saturation, while still capturing very weak signals from Raman scattering or fluorescence. As for some technological solutions, the H10721P-210 Hamamatsu photomultiplier modules, successfully tested in the CONCERNING and MARCO systems, are based on the same R9880U-210 metal package PMT that is being evaluated for CALIGOLA. Furthermore, the design of the beam expander in the CONCERNING lidar served as the basis for a candidate design for a reflective beam expander for the CALIGOLA mission, as an alternative to

refractive beam expanders that cannot collimate with the same efficiency laser light ranging from UV to NearIR, resulting in different divergences at the three used wavelengths.

Finally, the two deployable systems will be an extremely valuable resource for the satellite calibration and validation during both the commissioning and operational phases, whether through routine data collection or dedicated measurement campaigns.

Conclusions

This thesis has presented a comprehensive study on the development and application of Raman lidar systems for the measurements of compositional and thermodynamic properties of the atmosphere.

Two compact and transportable ground-based lidar prototypes, CONCERNING and MARCO, were developed in the frame of the PhD research effort, and after a period of test, deployed in a variety of national and international measurement campaigns, demonstrating their measurement capabilities. These systems utilize both rotational and vibrational Raman lidar techniques in the UV spectrum, incorporating advanced technologies for the laser emission, spectral selection, optical signal detection, and data acquisition. They are housed in sealed, rugged containers with fused-silica windows, allowing the operation in all weather conditions. Both can be controlled remotely, offering continuous and unattended measurement capabilities. The lidar MARCO successfully demonstrated for the first time the feasibility and performances of a Raman lidar based on a micro-pulse laser source. Ongoing and planned efforts will further enhance the capabilities of these two Raman lidar systems.

The two systems participated in three measurement campaigns. The WaLiNeAs project, focusing on the study of extreme precipitation events and on the enhancing of their predictability through the assimilation of water vapor profiles, highlighted the potential for a network of water vapor Raman lidars. The second campaign, BELLA, was centered on the characterization of the ABL. Finally, DECIPHER, that is dedicated to the study of phenomena of transport and mixing in mountain areas. Moreover, other measurement campaigns are planned in the near future, such as the Lidar-based Atmospheric Measurement at Pianosa (LAMP), dedicated to the study of marine aerosol and cloud interaction, and the second part of the DECIPHER campaign. On top of all the activities focused on the upgrade of the systems, future efforts will be dedicated to the reprocessing and analysis of the collected datasets in terms of meteorological process, atmospheric turbulence studies, climatological analysis.

A Raman lidar simulator was developed, and played a crucial role in defining the characteristics of the spectral selection devices needed for the application of the Raman lidar technique to measure CO_2 mixing ratio profiles, in evaluating the expected system performance, and in calibrating the mixing ratio measurements. Following the preliminary simulations, the CO_2 measurement capability was then implemented in the lidar CONCERNING. The measurements presented in this thesis, calibrated with an original technique and compared to independent measurements, demonstrate the system's promising performances. This advancement represents a significant step forward in the accuracy and reliability of atmospheric CO_2 measurements. Following the consolidation of the measurement and calibration techniques, future work will focus on studying the impact of the measured profiles on atmospheric process modeling. This

includes characterizing CO_2 vertical and temporal gradients from the forest floor to the canopy top, as well as examining land-atmosphere interactions and turbulent transport processes in the atmospheric boundary layer. Additionally, the potential scientific impact on climate models will be quantified. Furthermore, the influence of the measured CO_2 profiles on validating satellite products will also be assessed.

Regarding the future CALIGOLA satellite mission, this PhD research project led to the acquisition of useful know-how in the Raman lidar technique and contributed in various ways to the mission. The lidar simulator will be enhanced to form the foundation of a comprehensive end-to-end lidar simulator of the space-borne lidar. Additionally, the developed lidars have served as a testing platform for various state-of-the-art technological solutions and techniques that will be implemented in the CALIGOLA mission. Also, their measurement capabilities will be of great value for the calibration and validation of CALIGOLA's atmospheric products. Moreover, the compositional and thermodynamic measurements from the two ground-based lidars, when combined with CALIGOLA's data, could be used in future synergetic studies, enhancing our understanding of feedback and coupling mechanisms within Earth's biogeochemical cycles.

Bibliography

[1] IPCC (2013) Climate Change 2013: The Physical Science Basis. Contribution of Working Group I to the Fifth Assessment Report of the Intergovernmental Panel on Climate Change (Cambridge University Press).

[2] IPCC (2021) Climate Change 2021: The Physical Science Basis. Contribution of Working Group I to the Sixth Assessment Report of the Intergovernmental Panel on Climate Change (Cambridge University Press).

[3] Friedlingstein P, O'Sullivan M, Jones MW, Andrew RM, Bakker DCE, Hauck J, Landschützer P, Le Quéré C, Luijkx IT, Peters GP, Peters W, Pongratz J, Schwingshackl C, Sitch S, Canadell JG, Ciais P, Jackson RB, Alin SR, Anthoni P, Barbero L, Bates NR, Becker M, Bellouin N, Decharme B, Bopp L, Brasika IBM, Cadule P, Chamberlain MA, Chandra N, Chau T-T-T, Chevallier F, Chini LP, Cronin M, Dou X, Enyo K, Evans W, Falk S, Feely RA, Feng L, Ford DJ, Gasser T, Ghattas J, Gkritzalis T, Grassi G, Gregor L, Gruber N, Gürses Ö, Harris I, Hefner M, Heinke J, Houghton RA, Hurtt GC, Iida Y, Ilyina T, Jacobson AR, Jain A, Jarníková T, Jersild A, Jiang F, Jin Z, Joos F, Kato E, Keeling RF, Kennedy D, Klein Goldewijk K, Knauer J, Korsbakken JI, Körtzinger A, Lan X, Lefèvre N, Li H, Liu J, Liu Z, Ma L, Marland G, Mayot N, McGuire PC, McKinley GA, Meyer G, Morgan EJ, Munro DR, Nakaoka S-I, Niwa Y, O'Brien KM, Olsen A, Omar AM, Ono T, Paulsen M, Pierrot D, Pocock K, Poulter B, Powis CM, Rehder G, Resplandy L, Robertson E, et al. (2023) Global Carbon Budget 2023. Earth System Science Data 15(12):5301–5369. https://doi.org/10.5194/essd-15-5301-2023

[4] Stephens BB, Gurney KR, Tans PP, Sweeney C, Peters W, Bruhwiler L, Ciais P, Ramonet M, Bousquet P, Nakazawa T, Aoki S, Machida T, Inoue G, Vinnichenko N, Lloyd J, Jordan A, Heimann M, Shibistova O, Langenfelds RL, Steele LP, Francey RJ, Denning AS (2007) Weak Northern and Strong Tropical Land Carbon Uptake from Vertical Profiles of Atmospheric CO2. Science. Available at https://www.science.org/doi/abs/10.1126/science.1137004

[5] Gatti LV, Miller JB, D'Amelio MTS, Martinewski A, Basso LS, Gloor ME, Wofsy S, Tans P (2010) Vertical profiles of CO2 above eastern Amazonia suggest a net carbon flux to the atmosphere and balanced biosphere between 2000 and 2009. Tellus B: Chemical and Physical Meteorology 62(5). Available at https://b.tellusjournals.se/articles/10.1111/j.1600-0889.2010.00484.x

[6] Qiu R, ge H, Ma X, Sha Z, Tianqi S, Xu H, Zhang M (2020) CO2 Concentration, A Critical Factor Influencing the Relationship between Solar-induced Chlorophyll Fluorescence and Gross Primary Productivity. Remote Sensing 12:1377. https://doi.org/10.3390/rs12091377

[7] Dierer S, Arpagaus M, Seifert A, Avgoustoglou E, Dumitrache R, Grazzini F, Mercogliano P, Milelli M, Starosta K (2009) Deficiencies in quantitative precipitation forecasts: sensitivity studies using the COSMO model.

Meteorologische Zeitschrift:631–645. https://doi.org/10.1127/0941-2948/2009/0420

[8] Fourrié N, Nuret M, Brousseau P, Caumont O, Doerenbecher A, Wattrelot E, Moll P, Bénichou H, Puech D, Bock O, Bosser P, Chazette P, Flamant C, Di Girolamo P, Richard E, Saïd F (2019) The AROME-WMED reanalyses of the first special observation period of the Hydrological cycle in the Mediterranean experiment (HyMeX). Geoscientific Model Development 12(7):2657–2678. https://doi.org/10.5194/gmd-12-2657-2019

[9] Crook NA (1996) Sensitivity of Moist Convection Forced by Boundary Layer Processes to Low-Level Thermodynamic Fields. Monthly Weather Review 124(8):1767–1785. https://doi.org/10.1175/1520-0493(1996)124<1767:SOMCFB>2.0.CO;2

[10] Wulfmeyer V, Hardesty RM, Turner DD, Behrendt A, Cadeddu MP, Di Girolamo P, Schlüssel P, Baelen JV, Zus F (2015) A review of the remote sensing of lower tropospheric thermodynamic profiles and its indispensable role for the understanding and the simulation of water and energy cycles. Reviews of Geophysics 53(3):819–895. https://doi.org/10.1002/2014RG000476

[11] Di Girolamo P, Marchese R, Whiteman DN, Demoz BB (2004) Rotational Raman Lidar measurements of atmospheric temperature in the UV. Geophysical Research Letters 31(1). https://doi.org/10.1029/2003GL018342

[12] Whiteman DN, Rush K, Veselovskii I, Cadirola M, Comer J, Potter JR, Tola R (2007) Demonstration Measurements of Water Vapor, Cirrus Clouds, and Carbon Dioxide Using a High-Performance Raman Lidar. Journal of Atmospheric and Oceanic Technology 24(8):1377–1388. https://doi.org/10.1175/JTECH2058.1

[13] Lange D, Behrendt A, Wulfmeyer V (2019) Compact Operational Tropospheric Water Vapor and Temperature Raman Lidar with Turbulence Resolution. Geophysical Research Letters 46(24):14844–14853. https://doi.org/10.1029/2019GL085774

[14] Italian Space Agency (ASI) (2024) CALIGOLA mission. ASI. Available at https://www.asi.it/en/earth-science/caligola-mission/

[15] Riebesell M (1990) Raman lidar for the remote sensing of the water vapor and carbon dioxide profile in the troposphere (in German). PhD thesis (University of Hamburg).

[16] Ansmann A, Wandinger U, Riebesell M, Weitkamp C, Michaelis W (1992) Independent measurement of extinction and backscatter profiles in cirrus clouds by using a combined Raman elastic-backscatter lidar. Applied Optics 31(33):7113–7131. https://doi.org/10.1364/AO.31.007113

[17] Dionisi D (2006) Development of a Raman Lidar for the measurement of atmospheric CO2 concentration. Master’s degree thesis (Sapienza).

[18] Zhao P, Zhang Y, Wang L, Cao K, Su J, Hu S, Hu H (2008) Measurement of tropospheric CO2 and aerosol extinction profiles with Raman lidar. Chinese Optics Letters 6(3):157–160. https://doi.org/10.3788/COL20080603.0157

[19] Measures RM (1984) Laser remote sensing: Fundamentals and applications (John Wiley & Sons, Inc.), 1st Ed. Available at http://adsabs.harvard.edu/abs/1984wi...book.....M

[20] Bodhaine BA, Wood NB, Dutton EG, Slusser JR (1999) On Rayleigh Optical Depth Calculations. Journal of Atmospheric and Oceanic Technology 16:8.

[21] Daumont D, Brion J, Charbonnier J, Malicet J (1992) Ozone UV spectroscopy I: Absorption cross-sections at room temperature. Journal of Atmospheric Chemistry 15(2):145–155. https://doi.org/10.1007/BF00053756

[22] Voigt S, Orphal J, Burrows JP (2002) The temperature and pressure dependence of the absorption cross-sections of NO2 in the 250–800 nm region measured by Fourier-transform spectroscopy. Journal of Photochemistry and Photobiology A: Chemistry 149(1):1–7. https://doi.org/10.1016/S1010-6030(01)00650-5

[23] Rothman LS, Gordon IE, Babikov Y, Barbe A, Chris Benner D, Bernath PF, Birk M, Bizzocchi L, Boudon V, Brown LR, Campargue A, Chance K, Cohen EA, Coudert LH, Devi VM, Drouin BJ, Fayt A, Flaud J-M, Gamache RR, Harrison JJ, Hartmann J-M, Hill C, Hodges JT, Jacquemart D, Jolly A, Lamouroux J, Le Roy RJ, Li G, Long DA, Lyulin OM, Mackie CJ, Massie ST, Mikhailenko S, Müller HSP, Naumenko OV, Nikitin AV, Orphal J, Perevalov V, Perrin A, Polovtseva ER, Richard C, Smith MAH, Starikova E, Sung K, Tashkun S, Tennyson J, Toon GC, Tyuterev VlG, Wagner G (2013) The HITRAN2012 molecular spectroscopic database. Journal of Quantitative Spectroscopy and Radiative Transfer 130:4–50. https://doi.org/10.1016/j.jqsrt.2013.07.002

[24] Anderson GP, Clough SA, Kneizys FX, Chetwynd JH, Shettle EP (1986) AFGL (Air Force Geophysical Laboratory) atmospheric constituent profiles (0. 120km). Environmental research papers. (Air Force Geophysics Lab., Hanscom AFB, MA (USA)), AD-A-175173/4/XAB; AFGL-TR-86-0110. Available at https://www.osti.gov/biblio/6862535-afgl-air-force-geophysical-laboratory-atmospheric-constituent-profiles-environmental-research-papers

[25] Weitkamp C ed. (2005) Lidar: range-resolved optical remote sensing of the atmosphere (Springer, New York).

[26] She C-Y, Friedman JS (2022) Atmospheric Lidar Fundamentals: Laser Light Scattering from Atoms and Linear Molecules (Cambridge University Press, Cambridge). https://doi.org/10.1017/9781108968713

[27] Tejeda G, Maté B, Montero S (1995) Overtone Raman spectrum and molecular polarizability surface of CO2. The Journal of Chemical Physics 103(2):568–576. https://doi.org/10.1063/1.470091

[28] Lemus R, Sánchez-Castellanos M, Pérez-Bernal F, Fernández JM, Carvajal M (2014) Simulation of the Raman spectra of CO_2: Bridging the gap between

algebraic models and experimental spectra. The Journal of Chemical Physics 141(5):054306. https://doi.org/10.1063/1.4889995

[29] Inaba H, Kobayasi T (1972) Laser-Raman radar —Laser-Raman scattering methods for remote detection and analysis of atmospheric pollution. Opto-electronics 4(2):101–123. https://doi.org/10.1007/BF01421175

[30] Gray LD, Young AT (1969) Relative intensity calculations for carbon dioxide—IV: Calculations of the partition function for isotopes of CO2. Journal of Quantitative Spectroscopy and Radiative Transfer 9(5):569–589. https://doi.org/10.1016/0022-4073(69)90008-9

[31] Avila G, Fernández JM, Tejeda G, Montero S (2004) The Raman spectra and cross-sections of H2O, D2O, and HDO in the OH/OD stretching regions. Journal of Molecular Spectroscopy 228(1):38–65. https://doi.org/10.1016/j.jms.2004.06.012

[32] Avila G, Tejeda G, Fernández JM, Montero S (2003) The rotational Raman spectra and cross sections of H2O, D2O, and HDO. Journal of Molecular Spectroscopy 220(2):259–275. https://doi.org/10.1016/S0022-2852(03)00123-1

[33] Amplitude Laser Powerlite DLS-8000 Datasheet. Available at https://amplitude-laser.com/wp-content/uploads/2019/03/Powerlite-DLS-8000_ref-f.pdf

[34] Lumibird Merion MW Datasheet. Available at https://www.quantel-laser.com/tl_files/client/docs_produits/Merion%20MW_Specs_092022.pdf

[35] Koechner W (2006) Solid-state laser engineering (Springer, New York, NY), 6th rev. and updated ed.

[36] Jammu KS, John GESt, Welsh HL (1966) Pressure broadening of the rotational raman lines of some simple gases. Canadian Journal of Physics 44(4):797–814. https://doi.org/10.1139/p66-068

[37] Di Girolamo P, Behrendt A, Wulfmeyer V (2006) Spaceborne profiling of atmospheric temperature and particle extinction with pure rotational Raman lidar and of relative humidity in combination with differential absorption lidar: performance simulations. Applied Optics 45(11):2474. https://doi.org/10.1364/AO.45.002474

[38] NREL American Society for Testing and Materials (ASTM) G-173. Available at https://www.nrel.gov/grid/solar-resource/spectra-am1.5.html

[39] Henyey LG, Greenstein JL (1941) Diffuse radiation in the Galaxy. The Astrophysical Journal 93:70–83. https://doi.org/10.1086/144246

[40] Rozanov VV, Rozanov AV, Kokhanovsky AA, Burrows JP (2014) Radiative transfer through terrestrial atmosphere and ocean: Software package SCIATRAN. Journal of Quantitative Spectroscopy and Radiative Transfer 133:13–71. https://doi.org/10.1016/j.jqsrt.2013.07.004

[41] Rozanov VV, Dinter T, Rozanov AV, Wolanin A, Bracher A, Burrows JP (2017) Radiative transfer modeling through terrestrial atmosphere and ocean accounting for inelastic processes: Software package SCIATRAN. Journal of Quantitative Spectroscopy and Radiative Transfer 194:65–85. https://doi.org/10.1016/j.jqsrt.2017.03.009

[42] Mei L, Rozanov V, Rozanov A, Burrows JP (2023) SCIATRAN software package (V4.6): update and further development of aerosol, clouds, surface reflectance databases and models. Geoscientific Model Development 16(5):1511–1536. https://doi.org/10.5194/gmd-16-1511-2023

[43] Fontenla J, White OR, Fox PA, Avrett EH, Kurucz RL (1999) Calculation of Solar Irradiances. I. Synthesis of the Solar Spectrum. The Astrophysical Journal 518(1):480. https://doi.org/10.1086/307258

[44] NASA AERONET - Aerosol Robotic Network. Available at https://aeronet.gsfc.nasa.gov/

[45] Global Monitoring Laboratory NOAA Solar Calculator. Available at https://gml.noaa.gov/grad/solcalc/

[46] Wright RB (1973) Density effect on the Fermi resonance in gaseous CO2 by Raman scattering. The Journal of Chemical Physics 58(7):2893. https://doi.org/10.1063/1.1679594

[47] Di Girolamo P, Dionisi D, Cacciani M, Di Bernardino A, Franco N, Summa D, Di Paolantonio M, Iannarelli AM, Di Iorio T (2023) A Compact Raman Lidar for Atmospheric CO2 and Thermodynamic Profiling: The System CONCERNING. Proceedings of the 30th International Laser Radar Conference, eds Sullivan JT, Leblanc T, Tucker S, Demoz B, Eloranta E, Hostetler C, Ishii S, Mona L, Moshary F, Papayannis A, Rupavatharam K (Springer International Publishing, Cham), pp 531–537. https://doi.org/10.1007/978-3-031-37818-8_69

[48] International Electrotechnical Commission (2014) IEC 60825-1:2014 Safety of laser products - Part 1: Equipment classification and requirements. Available at https://webstore.iec.ch/en/publication/3587

[49] D'Amico G, Amodeo A, Mattis I, Freudenthaler V, Pappalardo G (2016) EARLINET Single Calculus Chain – technical – Part 1: Pre-processing of raw lidar data. Atmospheric Measurement Techniques 9(2):491–507. https://doi.org/10.5194/amt-9-491-2016

[50] Behrendt A, Nakamura T, Onishi M, Baumgart R, Tsuda T (2002) Combined Raman lidar for the measurement of atmospheric temperature, water vapor, particle extinction coefficient, and particle backscatter coefficient. Applied Optics 41(36):7657–7666. https://doi.org/10.1364/AO.41.007657

[51] Di Girolamo P, Cacciani M, Summa D, Scoccione A, De Rosa B, Behrendt A, Wulfmeyer V (2017) Characterisation of boundary layer turbulent processes by the Raman lidar BASIL in the frame of HD(CP)^2 Observational Prototype Experiment. Atmospheric Chemistry and Physics 17(1):745–767. https://doi.org/10.5194/acp-17-745-2017

[52] Ansmann A, Riebesell M, Wandinger U, Weitkamp C, Voss E, Lahmann W, Michaelis W (1992) Combined raman elastic-backscatter LIDAR for vertical profiling of moisture, aerosol extinction, backscatter, and LIDAR ratio. Applied Physics B Photophysics and Laser Chemistry 55(1):18–28. https://doi.org/10.1007/BF00348608

[53] Klett JD (1981) Stable analytical inversion solution for processing lidar returns. Applied Optics 20(2):211. https://doi.org/10.1364/AO.20.000211

[54] Fernald FG (1984) Analysis of atmospheric lidar observations: some comments. Applied Optics 23(5):652–653. https://doi.org/10.1364/AO.23.000652

[55] Di Girolamo P, Ambrico PF, Amodeo A, Boselli A, Pappalardo G, Spinelli N (1999) Aerosol observations by lidar in the nocturnal boundary layer. Applied Optics 38(21):4585–4595. https://doi.org/10.1364/AO.38.004585

[56] Flamant C, Chazette P, Caumont O, Di Girolamo P, Behrendt A, Sicard M, Totems J, Lange D, Fourrié N, Brousseau P, Augros C, Baron A, Cacciani M, Comerón A, De Rosa B, Ducrocq V, Genau P, Labatut L, Muñoz-Porcar C, Rodríguez-Gómez A, Summa D, Thundathil R, Wulfmeyer V (2021) A network of water vapor Raman lidars for improving heavy precipitation forecasting in southern France: introducing the WaLiNeAs initiative. Bulletin of Atmospheric Science and Technology 2(1):10. https://doi.org/10.1007/s42865-021-00037-6

[57] Météo-France Observations d'altitude (Radio sondages). Available at https://donneespubliques.meteofrance.fr/?fond=produit&id_produit=97&id_rubrique=33

[58] Senff C, Bösenberg J, Peters G (1994) Measurement of Water Vapor Flux Profiles in the Convective Boundary Layer with Lidar and Radar-RASS. Available at https://journals.ametsoc.org/view/journals/atot/11/1/1520-0426_1994_011_0085_mowvfp_2_0_co_2.xml

[59] Wulfmeyer V (1999) Investigation of Turbulent Processes in the Lower Troposphere with Water Vapor DIAL and Radar–RASS. Available at https://journals.ametsoc.org/view/journals/atsc/56/8/1520-0469_1999_056_1055_iotpit_2.0.co_2.xml

[60] Weather Research & Forecasting Model (WRF) Available at https://www.mmm.ucar.edu/models/wrf

[61] CNR-IMAA BELLA - Boundary layer Extensive campaign with muLti instrumentaL Analisys. CIAO - CNR IMAA Atmospheric Observatory. Available at https://ciao.imaa.cnr.it/bella-boundary-layer-extensive-campaign-with-multi-instrumental-analisys/

[62] Madonna F, Amodeo A, Boselli A, Cornacchia C, Cuomo V, D'Amico G, Giunta A, Mona L, Pappalardo G (2011) CIAO: the CNR-IMAA advanced observatory for atmospheric research. Atmospheric Measurement Techniques 4(6):1191–1208. https://doi.org/10.5194/amt-4-1191-2011

[63] Disentangling mechanisms controlling atmospheric transport and mixing processes over mountain areas at different space- and timescales (DECIPHER) TEAMx. Available at https://www.teamx-programme.org/projects/DECIPHER/

[64] CNR-ISP Col Margherita Observatory. Available at https://www.isp.cnr.it/index.php/en/research/other-activities/col-margherita

[65] Sherlock V, Hauchecorne A, Lenoble J (1999) Methodology for the independent calibration of Raman backscatter water-vapor lidar systems. Applied Optics 38(27):5816. https://doi.org/10.1364/AO.38.005816

[66] Muñoz-Porcar C, Comerón A, Sicard M, Barragan R, Garcia-Vizcaino D, Rodríguez-Gómez A, Rocadenbosch F, Granados-Muñoz MJ (2018) Calibration of Raman Lidar Water Vapor Mixing Ratio Measurements Using Zenithal Measurements of Diffuse Sunlight and a Radiative Transfer Model. IEEE Transactions on Geoscience and Remote Sensing 56(12):7405–7414. https://doi.org/10.1109/TGRS.2018.2851064

[67] OCO-2/OCO-3 Science Team, V. Payne, A. Chatterjee (2022) "OCO-2 Level 2 geolocated XCO2 retrievals results, physical model V11", Greenbelt, MD, USA, Goddard Earth Sciences Data and Information Services Center (GES DISC). Available at https://disc.gsfc.nasa.gov/datacollection/OCO2_L2_Standard_11.html

[68] ICOS - Integrated Carbon Observation System (2024) Available at https://www.icos-cp.eu/

[69] Di Girolamo P, Cosentino A, Longo F, Franco N, Dionisi D, Summa D, Lolli S, Suetta E, Perna A, Zoffoli S (2023) Introducing the Cloud Aerosol Lidar for Global Scale Observations of the Ocean-Land-Atmosphere System: CALIGOLA. Proceedings of the 30th International Laser Radar Conference, eds Sullivan JT, Leblanc T, Tucker S, Demoz B, Eloranta E, Hostetler C, Ishii S, Mona L, Moshary F, Papayannis A, Rupavatharam K (Springer International Publishing, Cham), pp 625–630. https://doi.org/10.1007/978-3-031-37818-8_80

[70] Behrenfeld MJ, Lorenzoni L, Hu Y, Bisson KM, Hostetler CA, Di Girolamo P, Dionisi D, Longo F, Zoffoli S (2023) Satellite Lidar Measurements as a Critical New Global Ocean Climate Record. Remote Sensing 15(23):5567. https://doi.org/10.3390/rs15235567

[71] Franco N (2024) An End-to-end simulator for the performance assessment of space Raman Lidar systems. Accepted: 2024-03-04T15:44:45Z (Università degli studi della Basilicata). Available at https://iris.unibas.it/handle/11563/176721?mode=simple

Publication List

1. Dionisi, D., Bucci, S., Cesarini, C., Colella, S., D'Alimonte, D., Di Ciolo, L., Di Girolamo, P., Di Paolantonio, M., Franco, N., Gostinicchi, G., Giuliano, G., Kajiyama, T., Organelli, E., Santoleri, R., Liberti, G.L.: Exploring the potential of Aeolus lidar mission for ocean color applications, Remote Sens. Environ, 313, 114341, https://doi.org/10.1016/j.rse.2024.114341, 2024.

2. D'Alimonte, D., Liberti, G. L., Di Paolantonio, M., Kajiyama, T., Franco, N., Di Girolamo, P., and Dionisi, D.: In-water lidar simulations: the ALADIN ADM-Aeolus backscattered signal at 355 nm, Opt. Express, OE, 32, 22781–22803, https://doi.org/10.1364/OE.510919, 2024.

3. Di Girolamo, P., Franco, N., Di Paolantonio, M., Summa, D., and Dionisi, D.: Atmospheric Thermodynamic Profiling through the Use of a Micro-Pulse Raman Lidar System: Introducing the Compact Raman Lidar MARCO, Sensors, 23, 8262, https://doi.org/10.3390/s23198262, 2023.

4. Tsekeri, A., Gialitaki, A., Di Paolantonio, M., Dionisi, D., Liberti, G. L., Fernandes, A., Szkop, A., Pietruczuk, A., Pérez-Ramírez, D., Granados Muñoz, M. J., Guerrero-Rascado, J. L., Alados-Arboledas, L., Bermejo Pantaleón, D., Bravo-Aranda, J. A., Kampouri, A., Marinou, E., Amiridis, V., Sicard, M., Comerón, A., Muñoz-Porcar, C., Rodríguez-Gómez, A., Romano, S., Perrone, M. R., Shang, X., Komppula, M., Mamouri, R.-E., Nisantzi, A., Hadjimitsis, D., Navas-Guzmán, F., Haefele, A., Szczepanik, D., Tomczak, A., Stachlewska, I. S., Belegante, L., Nicolae, D., Voudouri, K. A., Balis, D., Floutsi, A. A., Baars, H., Miladi, L., Pascal, N., Dubovik, O., and Lopatin, A.: Combined sun-photometer–lidar inversion: lessons learned during the EARLINET/ACTRIS COVID-19 campaign, Atmos. Meas. Tech., 16, 6025–6050, https://doi.org/10.5194/amt-16-6025-2023, 2023.

5. Di Paolantonio, M., Dionisi, D., and Liberti, G. L.: A semi-automated procedure for the emitter–receiver geometry characterization of motor-controlled lidars, Atmos. Meas. Tech., 15, 1217–1231, https://doi.org/10.5194/amt-15-1217-2022, 2022.

Abstracts in international conferences

1. M. Di Paolantonio, D. Dionisi, A. Di Bernardino, T. Di Iorio, N. Franco, G. Giuliano, A. M. Iannarelli, G. L. Liberti, D. Summa and P. Di Girolamo: CO2 profiling in the lower troposphere using the Raman lidar technique: preliminary results, 31st International Laser Radar Conference (ILRC), Landshut, Germany, 23-28 June 2024.

2. D. Lange, T. Schwitalla, A. Behrendt, C. Flamant, P. Chazette, V. Wulfmeyer, O. Caumont, P. Di Girolamo, M. Sicard, J. Totems, F. Laly, J. Lagarrigue, N. Fourrié, P. Brousseau, C. Augros, A. Baron, N. Franco, M. Di Paolantonio, M. Cacciani, A. Comerón, B. De Rosa, V. Ducrocq, P. Genau, L. Labatut, C. Muñoz Porcar, A. Rodríguez Gómez, D. Summa, J.L. Gómez-Amo, P. Catalán, M.P. Utrillas: Assimilation of temperature and water-vapor mixing-ratio lidar profiles in WRF, 31st International Laser Radar Conference (ILRC), Landshut, Germany, 23-28 June 2024.

3. Giuliano, G., Dionisi, D., Di Paolantonio, M., Liberti, G. L.: Lidar system upgrade at Atmospheric Rome joinT supersitE (ARTE), 31st International Laser Radar Conference (ILRC), Landshut, Germany, 23-28 June 2024.

4. Dionisi, D., Di Paolantonio, M., D'Acunzo, E., Giuliano, G., Liberti, G. L., Volpe, G., N. Franco, Andrisani, A., Venafra, S., Zoffoli, S. and Di Girolamo, P.: Assessing the Ocean Color observation capability of the CALIGOLA mission: the PROTEO project, 31st International Laser Radar Conference (ILRC), Landshut, Germany, 23-28 June 2024.

5. P. Di Girolamo, D. Dionisi, N. Franco, M. Di Paolantonio, D. Summa, S. Lolli, L. Mona, R. Santoleri, S. Zoffoli, F. Tataranni, S. Venafra, T. Scopa, F. Longo, R. Votta, V. Sacchieri, F. Coppola, A. Perna, A. Cosentino, Y. Hu, C. A. Hostetler, T. Thorsen, J. Smith, M. J. Behrenfeld, S. Braun, B. Holz, G. Mace, H. Maring, L. Lorenzoni, S. R. Hall, C. R. Trepte: The CALIGOLA Mission: An overview of the present status and the forthcoming steps, 31st International Laser Radar Conference (ILRC), Landshut, Germany, 23-28 June 2024.

6. D. Summa, G. D'Amico, I. Gandolfi, M. Di Paolantonio, D. Dionisi, M. Rosoldi, B. De Rosa, and P. Di Girolamo: Latent Heat Flux and TKE measurements from the combined use of Water Vapour Raman and Wind Doppler Lidars during WaLiNeas Campaign, 31st International Laser Radar Conference (ILRC), Landshut, Germany, 23-28 June 2024.

7. M. Di Paolantonio, P. Di Girolamo, D. Dionisi, A. Di Bernardino, T. Di Iorio, N. Franco, A. M. Iannarelli, G. L. Liberti, D. Summa: Profiling of CO2 mixing ratio with Raman lidar: preliminary results, European Lidar Conference 2023, Cluj-Napoca, Romania, 13-15 September 2023.

8. Summa, D., D'amico, G., Gandolfi, I., Franco, N., Di Paolantonio, M., Rosoldi, M., De Rosa, B., and Di Girolamo, P.: Latent Heat Flux by Raman Lidar and Wind

Lidar system during Walineas Campaign., EGU General Assembly 2024, Vienna, Austria, 14–19 Apr 2024, EGU24-3097, https://doi.org/10.5194/egusphere-egu24-3097, 2024.

9. Di Girolamo, P., Franco, N., Dionisi, D., Di Paolantonio, M., Summa, D., Lolli, S., Mona, L., Santoleri, R., Zoffoli, S., Tataranni, F., Scopa, T., Longo, F., Sacchieri, V., Perna, A., Cosentino, A., Hu, Y., Behrenfeld, M. J., Hostetler, C. A., Hall, S. R., and Trepte, C. R.: An overview of the Cloud and Aerosol Lidar for Global Scale Observations of the Ocean-Land-Atmosphere System, EGU General Assembly 2024, Vienna, Austria, 14–19 Apr 2024, EGU24-4039, https://doi.org/10.5194/egusphere-egu24-4039, 2024.

10. Di Girolamo, P., Franco, N., Di Paolantonio, M., Summa, D., Dionisi, D., Di Bernardino, A., Iannarelli, A. M., and Di Iorio, T.: Several months of continuous operation of two thermodynamic Raman lidars in the frame of WaLiNeAs, EGU General Assembly 2023, Vienna, Austria, 24–28 Apr 2023, EGU23-7775, https://doi.org/10.5194/egusphere-egu23-7775, 2023.

11. Di Paolantonio, M., Di Girolamo, P., Dionisi, D., Di Bernardino, A., Di Iorio, T., Franco, N., Giuliano, G., Iannarelli, A. M., Liberti, G. L., and Summa, D.: Performance Simulation and Preliminary Measurements of a Raman Lidar for the Retrieval of CO2 Atmospheric Profiles, EGU General Assembly 2023, Vienna, Austria, 24–28 Apr 2023, EGU23-16149, https://doi.org/10.5194/egusphere-egu23-16149, 2023.

12. Franco, N., Di Girolamo, P., Summa, D., Di Paolantonio, M., and Dionisi, D.: Preliminary Studies and Performance Simulations in support of the mission “CALIGOLA”, EGU General Assembly 2023, Vienna, Austria, 24–28 Apr 2023, EGU23-16695, https://doi.org/10.5194/egusphere-egu23-16695, 2023.

13. Dionisi, D., Bucci, S., Cesarini, C., Colella, S., D'Alimonte, D., Di Ciolo, L., Di Girolamo, P., Di Paolantonio, M., Franco, N., Gostinicchi, G., Kajiyama, T., Liberti, G. L., Organelli, E., and Santoleri, R.: Ocean color through satellite lidars: the COLOR project, EGU General Assembly 2023, Vienna, Austria, 24–28 Apr 2023, EGU23-16196, https://doi.org/10.5194/egusphere-egu23-16196, 2023.

14. M. Di Paolantonio, P. Di Girolamo, D. Dionisi, M. Cacciani, A. Di Bernardino, T. Di Iorio, N. Franco, A. M. Iannarelli, G. L. Liberti, D. Summa: Performance Simulation of a Raman Lidar for the Retrieval of CO2 Atmospheric Profiles. In: Sullivan, J.T., et al. Proceedings of the 30th International Laser Radar Conference. ILRC 2022. Springer Atmospheric Sciences. Springer, Cham. https://doi.org/10.1007/978-3-031-37818-8_15, 2023.

15. D. Dionisi, S. Bucci, C. Cesarini, S. Colella, D. D’Alimonte, L. Di Ciolo, P. Di Girolamo, M. Di Paolantonio, N. Franco, G. Giuliano, G. Gostinicchi, T. Kajiyama, G. L. Liberti, E. Organelli, R. Santoleri: First results of the COLOR (CDOM-proxy retrieval from aeOLus ObseRvations) project. In: Sullivan, J.T., et al. Proceedings of the 30th International Laser Radar Conference. ILRC 2022. Springer Atmospheric Sciences. Springer, Cham. https://doi.org/10.1007/978-3-031-37818-8_77, 2023.

16. P. Di Girolamo, D. Dionisi, M. Cacciani, A. Di Bernardino, N. Franco, D. Summa, M. Di Paolantonio, A. M. Iannarelli, T. Di Iorio: COmpact RamaN lidar for Atmospheric CO2 and ThERmodyNamic ProfilING - CONCERNING. In: Sullivan, J.T., et al. Proceedings of the 30th International Laser Radar Conference. ILRC 2022. Springer Atmospheric Sciences. Springer, Cham. https://doi.org/10.1007/978-3-031-37818-8_69, 2023.

17. M. Di Paolantonio, D. Dionisi and G. L. Liberti: Alignment optimization and overlap function estimation in stepper motor controlled lidars, European Lidar Conference 2021, Granada, Spain, 16-18 November 2021, https://granada-en.congresoseci.com/elc2021/elc2021_proceedings_book_final!, 2021.

18. D. Dionisi, S. Bucci, C. Cesarini, S. Colella, D. D'Alimonte, L. Di Ciolo, P. Di Girolamo, M. Di Paolantonio, N. Franco, G. Gostinicchi, T. Kajiyama, G. L. Liberti, E. Organelli and R. Santoleri: COLOR: CDOM-proxy retrieval from aeOLus ObseRvations, European Lidar Conference 2021, Granada, Spain, 16-18 November 2021, https://granada-en.congresoseci.com/elc2021/elc2021_proceedings_book_final!, 2021.

19. Tsekeri, A. Gialitaki, M. Di Paolantonio, D. Dionisi, G. L. Liberti, A. Fernandes, A. Szkop, A. Pietruczuk, D. Pérez-Ramírez, M. J. Granados Muñoz, J. L. Guerrero-Rascado, L. Alados-Arboledas, D. Bermejo Pantaleón, J. A. Bravo-Aranda,E. Marinou, V. Amiridis, A. Comerón, C. Muñoz-Porcar, A. Rodríguez-Gómez, M. Sicard, S. Romano, M.R. Perrone, X.Shang, M. Komppula, R. E. Mamouri, A. Nisantzi, D. Hadjimitsis, F. Navas-Guzmán, A. Haefele, I.S. Stachlewska, D.Szczepanik, R. Fortuna, B. Livio, D. Nicolae, P. Fréville, J. L. Baray, K. Eswaran, K. A. Voudouri, D. Balis, A. Floutsi, H.Baars, L. Miladi, N. Pascal, Q. Hu, P. Goloub, O. Dubovik, and A. Lopatin: Profiling of the anthropogenic aerosols in Europe during the ACTRIS/EARLINET COVID-19 campaign, European Lidar Conference 2021, Granada, Spain, 16-18 November 2021, https://granada-en.congresoseci.com/elc2021/elc2021_proceedings_book_final!, 2021.